Lithos 284–285 (2017) 560–577

Contents lists available at ScienceDirect

Lithos

journal homepage: www.elsevier.com/locate/lithos

Geochemistry of komatiites and basalts from the Rio das Velhas and Pitangui greenstone belts, São Francisco Craton, Brazil: Implications for the origin, evolution, and tectonic setting

Sanjeet K. Verma [a,*], Elson P. Oliveira [b], Paola M. Silva [b], Juan A. Moreno [b], Wagner S. Amaral [b]

[a] División de Geociencias Aplicadas, Instituto Potosino de Investigación Científica y Tecnológica (IPICYT), Camino a la Presa San José 2055, San Luis Potosí 78216, Mexico
[b] Department of Geology and Natural Resources, Institute of Geosciences, PO Box 6152, University of Campinas – UNICAMP, 13083-970 Campinas, SP, Brazil

ARTICLE INFO

Article history:
Received 3 February 2017
Accepted 30 April 2017
Available online 17 May 2017

Keywords:
Komatiites
High-Mg basalts
Basalts
Geochemistry
Greenstone belt
Tectonic setting

ABSTRACT

The Neoarchean Rio das Velhas and Pitangui greenstone belts are situated in the southern São Francisco Craton, Minas Gerais, Brazil. These greenstone belts were formed between ca. 2.79–2.73 Ga, and consist mostly of mafic to ultramafic volcanics and clastic sediments, with minor chemical sediments and felsic volcanics that were metamorphosed under greenschist facies. Komatiites are found only in the Rio das Velhas greenstone belt, which is composed of high-MgO volcanic rocks that have been identified as komatiites and high-Mg basalts, based on their distinctive geochemical characteristics. The Rio das Velhas komatiites are composed of tremolite + actinolite + serpentine + albite with a relict spinifex-texture. The Rio das Velhas komatiites have a high magnesium content ($(MgO)_{adj} \geq 28$ wt.%), an Al-undepleted Munro-type [$(Al_2O_3/TiO_2)_{adj}$ and $(CaO/Al_2O_3)_{adj}$] ratio ranging from 27 to 47 and 0.48 to 0.89, relatively low abundances of incompatible elements, a depletion of light rare earth elements (LREE), a pattern of non-fractionated heavy rare- earth elements (HREE), and a low $(Gd/Yb)_{PM}$ ratio (≤1.0). Negative Ce anomalies suggest that alteration occurred during greenschist facies metamorphism for the komatiites and high-Mg basalts. The low [$(Gd/Yb)_{PM} < 1.0$] and [$(CaO/Al_2O_3)_{adj} < 0.9$)], high [$(Al_2O_3/TiO_2)_{adj} > 18$] and high HREE, Y, and Zr content suggest that the Rio das Velhas komatiites were derived from the shallow upper mantle without garnet involvement in the residue. The chemical compositions [$(Al_2O_3/TiO_2)_{adj}$, $(FeO)_{adj}$, $(MgO)_{adj}$, $(CaO/Al_2O_3)_{adj}$, Na, Th, Ta, Ni, Cr, Zr, Y, Hf, and REE] indicate that the formation of the komatiites, high-Mg basalts and basalts occurred at different depths and temperatures in a heterogeneous mantle. The komatiites and high-Mg basalts melted at liquidus temperatures of ~1450–1550 °C. The Pitangui basalts are enriched in the highly incompatible LILE (large-ion lithophile elements) relative to the moderately incompatible HFS (high field strength) elements. The Zr/Th ratio ranging from 76 to 213 and the relationship between the Nb/Th and Th/Yb ratios indicate that there is no crustal contamination in the Pitangui greenstone basalts. New multi-dimensional discrimination diagrams and conventional normalized multi-element diagrams indicate an island arc (IA) setting for the komatiites and high-Mg basalts from the Rio das Velhas and a mid ocean-ridge (MOR) to IA setting for the basalts from the Pitangui greenstone belts.

1. Introduction

One of the largest shields in the world is the Brazilian Shield, which is also known as the South American Platform. The important parts of this platform are Neoproterozoic orogenic belts and cratons (Almeida et al., 1981, 2000; Hartmann and Delgado, 2001; Hartmann et al., 2008) that are mainly divided into three cratonic bodies: the Amazon Craton (Cordani and Teixeira, 2007; Geraldes et al., 2015; Santos et al., 2000; Tassinari et al., 2000; Teixeira et al., 2010; Tohver et al., 2004), the São Francisco Craton (Almeida, 1977; Delgado et al., 1994; Mascarenhas, 1981; Teixeira et al., 1996, 2015), and the Rio de la Plata Craton (Basei et al., 2000; Oyhantçabal et al., 2011; Rapela et al., 2007; Sánchez Bettucci et al., 2010). Besides these cratonic domains, smaller cratonic fragments occur such as the São Luís Craton (Klein and Moura, 2008; Klein et al., 2005; Sadowski, 2000) and the Luís Alves Craton (Basei et al., 2000; Cordani et al., 2000; Fuck et al., 2008). The Amazonian craton is the largest, and comprises Archean and Proterozoic terrains and has remained tectonically stable since the Neoproterozoic. It has been subdivided into several provinces based on their ages (Cordani and Teixeira, 2007; Santos et al., 2000; Tassinari and Macambira, 1999; Teixeira et al., 1989, 2010). The São Francisco Craton

* Corresponding author.
E-mail addresses: sanjeet.verma@ipicyt.edu.mx, sanjeet_vrm@yahoo.com (S.K. Verma), elson@ige.unicamp.br (E.P. Oliveira), paola.melo7@gmail.com (P.M. Silva), jmoreno_2@ugr.es (J.A. Moreno), wamaral@ige.unicamp.br (W.S. Amaral).

http://dx.doi.org/10.1016/j.lithos.2017.04.024
0024-4937/

is surrounded by Neoproterozoic orogenic belts, is one of the largest cratonic domains in eastern Brazil, and represents a crustal tangibility during the Brasiliano Orogeny, which occurred 630–500 Ma ago, during the amalgamation of West Gondwana (Alkmim et al., 2001; Almeida, 1977; Almeida et al., 1981; Campos and Carneiro, 2008; Cordani et al., 2000; Tohver et al., 2006; Trompette, 1994). This craton is subdivided into several Archean to Palaeoproterozoic blocks: Gavião, Guanambi-Correntina, Jequié, Mairi, Serrinha, and Itabuna-Salvador-Curaça (Barbosa and Sabaté, 2004; Ledru et al., 1997; Oliveira et al., 2010; Teixeira and Figueiredo, 1991; Teixeira et al., 1996, 2010, 2017a, 2017b). The Rio de la Plata Craton is mainly located in Uruguay, and extends into southern Brazil in the form of many cratonic fragments in the Neoproterozoic belts (Oyhantçabal et al., 2011; Rapela et al., 2007).

Archean greenstone belts consist of metamorphosed mafic to ultramafic volcanic sequences with associated sedimentary rocks and minor quantities of intermediate to felsic igneous rocks. High-Mg volcanic rocks, particularly komatiites and basalts are more abundant in Archean greenstone belts as compare than felsic rocks. Komatiites and basalts provide a means of constraining both mantle composition and magma generation temperature in time (Condie, 2015; Condie et al., 2016; Hofmann, 1988, 1997). The komatiites and basalts allow us to track these properties of the mantle back to at least 3.8 Ga (Arndt et al., 2008; Abbott et al., 1994; Herzberg and O'Hara, 1998). In this context, numerous studies have been done on komatiites from southern Africa, Australia, Brazil, Canada, Finland and India (Arndt et al., 1989; Arndt et al., 2008; Barnes et al., 1988; Chavagnac, 2004; Dostal and Mueller, 2013; Jahn et al., 1982; Rajamani et al., 1985; Jayananda et al., 2016; Konnunaho et al., 2013; Manikyamba et al., 2013; Mole et al., 2014; Polat et al., 1999; Polat and Kerrich, 2000; Saha et al., 2015; Stiegler et al., 2010; Waterton et al., 2017). Furthermore, the geodynamic evolution of Archean komatiite magma has been the subject of much discussion—that is whether komatiite magmas are generated by the anhydrous melting of deep mantle or the wet melting of shallow mantle (Arndt, 2003; Parman et al., 1997; Polat et al., 1999). Similarly, the tectonic context of magma generation of komatiites is still a matter of debate (Arndt et al., 2008; Parman et al., 2004), although many researchers have suggested that komatiite magmas are derived from anomalously hot mantle plumes (Arndt et al., 2008; Herzberg, 1995; Herzberg et al., 2010).

The study areas, the Rio das Velhas and Pitangui greenstone belts, are located in the southern part of the São Francisco Craton. Earlier studies of the Rio das Velhas greenstone belt were conducted mainly on field relationships and the petrographic, geochemical, and geochronological characteristics of basaltic and sedimentary rocks (Hartmann et al., 2006; Oliveira et al., 2011; Romano et al., 2013; Teixeira et al., 2015; Zucchetti et al., 2000a, 2000b). However, no detailed geochemical studies have been performed on komatiites and high-Mg basalts. Similarly, there are no available studies on the geochemistry and petrogenesis of the basalts of the Pitangui greenstone belt. Therefore, in this work, we present the field-relationships and geochemistry of ultramafic to mafic volcanic rocks of both the Rio das Velhas and Pitangui greenstone belts to discuss their petrogenesis, Archean mantle evolution and tectonic setting.

2. Geological setting

The São Francisco Craton is mainly divided into two parts: the northern craton and the southern craton. The northern part has been divided into four crustal blocks: Jequié, Gavião, Serrinha, and Itabuna-Salvador-Curaça (Barbosa and Sabaté, 2004). The southern part consists of several gneiss complexes (Bonfim, Passa Tempo, Divinópolis, Campo Belo, Guanhães, Bação, Belo Horizonte, Santa Bárbara, Caeté), greenstone belts (Rio das Velhas, Pitangui, Piumhi, Rio Paraúna, Fortaleza de Minas, Barbacena), and the Mineiro orogen (Alkmim and Teixeira, 2017; Moreno et al., 2017; Teixeira et al., 2017a, 2017b and references therein).

The Archean greenstone belts of the São Francisco Craton (Fig. 1a) are situated in the southern part of the craton (in the state of Minas Gerais) and in the Gavião block in the north (Cunha and Fróes, 1994; Lobato et al., 2001a; Menezes Leal et al., 2015; Teixeira et al., 2017a, 2017b). The Rio das Velhas (Fig. 1a) and Pitangui (Fig. 1b) greenstone belts are located in the southern part of the São Francisco Craton, (Baltazar and Zucchetti, 2007; Dorr, 1969; Teixeira et al., 2017a, 2017b; Vial et al., 2007; Zucchetti et al., 2000a, 2000b).

The Rio das Velhas greenstone belt consists of the Nova Lima and Maquiné Groups. From bottom to top, the Nova Lima Group is divided into five main lithofacies units (Baltazar and Zucchetti, 2007): Unit 1, mafic to ultramafic volcanic rocks with minor felsic volcanics; Unit 2, sedimentary and volcano-chemical sedimentary rocks; Unit 3, upper clastic-chemical sedimentary rocks; Unit 4, volcaniclastic rocks; and Unit 5, resedimented sedimentary rocks. The Nova Lima Group clastic sediments are in gradational contact with the overlying Maquiné Group—a 2000-m-thick sequence of phyllite and quartz–phyllite of the Palmital Formation (O'Rourke, 1957) and quartz schist, conglomerate, phyllite and greywacke of the Casa Forte Formation (Gair, 1962). Massive komatiites to pillowed komatiitic basalts occur in Unit 1 above the Nova Lima Group (Baltazar and Zucchetti, 2007; Zucchetti et al., 2000a, 2000b). The massive komatiites are characterized by a spinifex texture, layers with cumulus olivine/intercumulus orthopyroxene, and a layer of lahar-type breccia (Zucchetti et al., 2000a, 2000b). The pillowed komatiitic basalts are locally interleaved with marine carbonaceous sediments (Schrank et al., 1990). The pillowed basalt volcanism and carbonate precipitation were followed by the submarine deposition of banded iron formations (BIFs) and pelites (which are covered with sandstone-greywacke), a sequence of conglomerate-greywacke, and pelite-greywacke. Whole-rock Sm–Nd analyses indicate an age of 2927 ± 180 Ma for the basaltic rocks (Lobato et al., 2001b), whereas U–Pb and Pb–Pb zircon analyses yielded ages of 3035 Ma, 2930 Ma, and 2800 Ma for the felsic volcanism (Lobato et al., 2001b; Noce et al., 2002, 2005). Furthermore, Machado et al. (1992) explained that the felsic volcanism took place between 2776 and 2772 Ma. Later, Carneiro (1992) described this age interval as being related to the Rio das Velhas Orogenic Event, in which Archean crust was formed and other volcanism occurred. The clastic sedimentary rocks of the upper unit of the greenstone belt are dominated by greywacke–argillite sequences. The Maquiné Group consists of sandstones and conglomerates that overlie the Nova Lima Group. Moreira et al. (2016) constrained a maximum depositional age of 2730 Ma for the sediments of the Maquiné Group.

The Pitangui greenstone belt was divided into two units by Frizzo et al. (1991). The basal unit consists of mafic and ultramafic meta-igneous rocks approximately 200 m thick. The upper unit consists of metavolcanic rocks (i.e., rhyolite to andesite) with a strong contribution of pyroclastic volcanics and metasedimentary rocks consisting of carbonaceous phyllites, BIFs and ironstones. The thickness of this unit is about 2000 m. Silva (2016) and Silva et al. (under review) presented new U–Pb zircon ages for the rocks of the Pitangui greenstone belt and nearby basement. The basement gneiss was dated at 2876 ± 7 Ma, whereas a metabasalt and metagabbro from the greenstone belt yielded ages of 2771 ± 18 Ma and 2740 ± 36 Ma, respectively. The youngest detrital zircon population in two metasedimentary rocks (slate and phyllite) indicated an average age of 2720 Ma (n = 8 grains) and three other grains showed an average age of approximately 2670 Ma. Recently, Soares et al. (2017) divided the belt into three units: a lower unit of predominantly metavolcanic ultramafic and mafic rocks interbedded with thinner metasedimentary intervals of BIFs, turbiditic metasandstones and metapelites; a middle unit of turbiditic metasediments interbedded with metavolcanic intermediate rocks, minor BIFs, and quartzites; and an upper unit composed of quartzites and polymictic metaconglomerates. According to Soares et al. (2017), the rocks from all three units were metamorphosed under upper-greenschist to lower-amphibolite facies and are bounded by domes composed of Tonalite-Trondhjemite-Granodiorite (TTG) and late- to post-tectonic alkaline granitoids. U–Pb ages of detrital zircon grains from the lower-unit metasandstone indicate a maximum depositional age of 2859 ± 11 Ma (Soares et al., 2017).

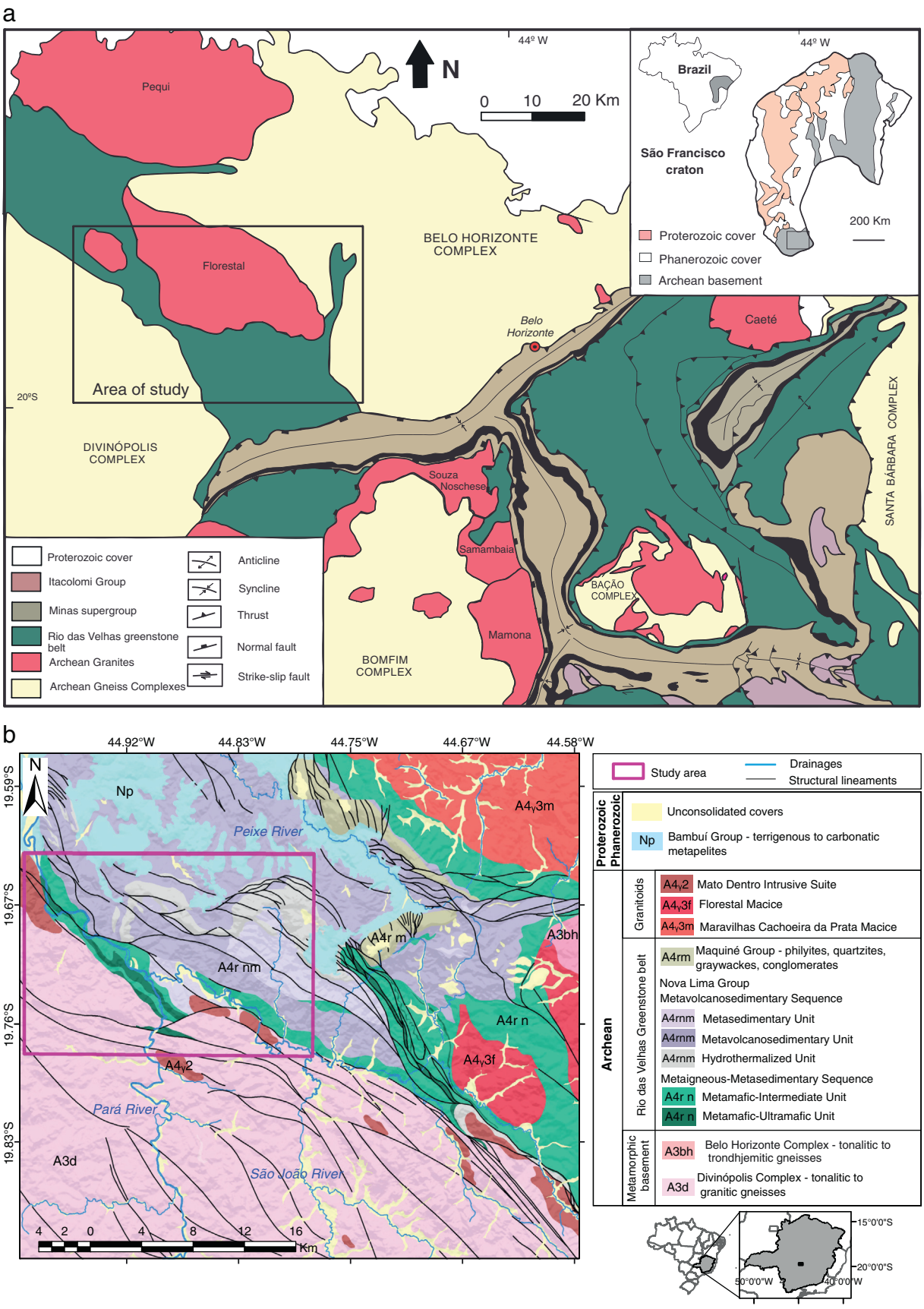

Fig. 1. a. Simplified geologic map of the Rio das Velhas Supergroup, São Francisco Craton, Brazil (Modified after Zucchetti et al. (2000a, 2000b)). b. Simplified geologic map of the Pitangui greenstone belt, São Francisco Craton, Brazil.
Adapted from Romano (2007).

Table 1
Representative whole rock compositions of komatiites and basalts from the greenstone belt, São Francisco craton, Brazil. Major elements in weight percent and trace elements in ppm.

Sample	15MGEO-1A	15MGEO-1B	15MGEO-1C	15MGEO-1D	15MGEO-5A	15MGEO-5B	15MGEO-5C	15MGEO-5D	15MGEO-2A	15MGEO-2B	15MGEO-2C	15MGEO-2E	15MGEO-3
	Rio das Velhas greenstone belt												
Rock unit	Komatiite	Komatiite	Komatiite	Komatiite	Komatiite	Komatiite	Komatiite	Komatiite	High-Mg basalt	High-Mg basalt	High-Mg basalt	High-Mg basalt	High-Mg basalt
Locality	Morro do Onça	Morro do Onça	Morro do Onça	Morro do Onça	Rio das Velhas	Rio das Velhas	Rio das Velhas	Rio das Velhas	Caeté-Sabara	Caeté-Sabara	Caeté-Sabara	Caeté-Sabara	Caeté-Sabara
Long. (°W):	44.36	44.36	44.36	44.36	43.44	43.44	43.44	43.44	43.69	43.69	43.69	43.69	43.68
Lat. (°S):	20.32	20.32	20.32	20.32	20.04	20.04	20.04	20.04	19.89	19.89	19.89	19.89	19.92
SiO_2	42.09	40.98	40.33	42.39	35.71	35.54	38.84	36.77	39.3	38.17	39.31	39.79	39.87
TiO_2	0.206	0.14	0.138	0.215	0.15	0.134	0.141	0.14	0.097	0.04	0.078	0.103	0.206
Al_2O_3	6.27	3.87	3.89	6.29	7.12	5.78	5.85	5.37	1.32	0.73	0.85	1.21	2.3
Fe_2O_3	10.84	9.95	9.33	11.41	9.69	7.18	7.91	7.39	10.98	14.91	12.13	10.36	10.93
MnO	0.152	0.12	0.121	0.149	0.169	0.142	0.122	0.134	0.14	0.115	0.129	0.134	0.113
MgO	26.88	32.56	33.36	26.1	27.81	31.89	30.73	32.66	35.6	34.55	35.52	36.07	34.55
CaO	5.44	1.89	1.9	5.35	6.34	3.92	3.63	2.88	0.04	0.03	0.02	0.02	0.05
Na_2O	0.29	0.04	0.03	0.21	0.05	0.02	0.02	0.01	0.02	0.02	0.02	0.02	0.02
K_2O	0.06	0.02	0.02	0.04	0.03	0.02	0.03	0.02	0.01	0.01	0.01	0.01	0.01
P_2O_5	0.039	0.022	0.029	0.054	0.059	0.023	0.016	0.022	0.027	0.017	0.02	0.017	0.038
LOI	7.02	9.41	9.86	6.81	12.59	14.41	12.3	13.68	11.14	10.53	10.87	11.2	10.81
Total	99.3	99	99	99	99.7	99	99.6	99.1	98.7	99.1	98.9	98.9	98.9
Adj Value													
$(SiO_2)_{adj}$	46.08	46.18	45.65	46.46	41.39	42.30	44.85	43.39	45.38	43.73	45.15	45.81	45.74
$(TiO_2)_{adj}$	0.23	0.16	0.16	0.24	0.17	0.16	0.16	0.17	0.11	0.05	0.09	0.12	0.24
$(Al_2O_3)_{adj}$	6.86	4.36	4.40	6.89	8.25	6.88	6.76	6.34	1.52	0.84	0.98	1.39	2.64
$(Fe_2O_3)_{adj}$	1.81	1.71	1.61	1.91	1.34	1.02	1.09	1.04	1.93	2.03	2.13	1.82	1.91
$(FeO)_{adj}$	9.05	8.55	8.05	9.54	8.90	6.78	7.24	6.91	9.67	13.54	10.63	9.10	9.56
$(MnO)_{adj}$	0.17	0.14	0.14	0.16	0.20	0.17	0.14	0.16	0.16	0.13	0.15	0.15	0.13
$(MgO)_{adj}$	29.43	36.69	37.76	28.61	32.24	37.96	35.49	38.54	41.11	39.59	40.80	41.53	39.64
$(CaO)_{adj}$	5.96	2.13	2.15	5.86	7.35	4.67	4.19	3.40	0.05	0.03	0.02	0.02	0.06
$(Na_2O)_{adj}$	0.32	0.05	0.03	0.23	0.06	0.02	0.02	0.01	0.02	0.02	0.02	0.02	0.02
$(K_2O)_{adj}$	0.07	0.02	0.02	0.04	0.03	0.02	0.03	0.02	0.01	0.01	0.01	0.01	0.01
$(P_2O_5)_{adj}$	0.04	0.02	0.03	0.06	0.07	0.03	0.02	0.03	0.03	0.02	0.02	0.02	0.04
Total	100	100	100	100	100	100	100	100	100	100	100	100	100
Ba	2.31	1.96	2.38	7.04	4.74	12.12	3.72	4.29	3.08	3.11	6.79	3.28	20.03
Be	0.09	0.11	0.04	0.08		0.02			0.08	0.08	0.08		0.33
Co	89.62	100.61	103.48	96.43	80.39	76.50	70.63	73.68	121.31	130.89	172.15	128.11	145.65
Cr	3955.58	2958.40	2799.20	4093.88	3584.55	3931.79	3678.53	3333.82	4407.94	2681.29	3871.38	4514.95	5360.64
Cs	1.54	1.21	0.85	1.39	0.83	1.28	1.59	1.10	0.80	0.17	0.18	0.24	0.24
Cu	15.26	6.23	23.17	34.95	0.64	0.70	0.83	0.80	10.13	1.31	7.80	4.85	10.62
Ga	5.86	3.76	3.68	5.26	4.73	3.80	3.97	3.51	2.24	1.37	1.59	1.66	3.20
Hf	0.40	0.26	0.21	0.37	0.23	0.16	0.19	0.10	0.20	0.09	0.10	0.12	0.38
Li	5.65	3.87	3.24	5.30	15.89	25.81	28.47	23.26	0.28	0.24	0.25	0.23	0.31
Nb	0.41	0.36	0.31	0.32	0.04	0.05	0.07	0.04	0.23	0.40	0.18	0.82	0.51
Ni	1050.94	1815.22	1989.41	1033.67	871.07	1212.75	1205.34	1266.44	2552.64	2730.57	2943.34	2911.53	2738.07
Pb	7.52	2.47	0.50	1.05	0.27	0.76	0.20	0.24	1.10	0.61	0.56	0.99	0.59
Rb	1.83	0.68	0.57	1.44	1.08	2.61	1.13	0.77	0.28	0.89	0.30	0.31	0.41
Sb	0.18	0.04	0.03	0.07	5.22	7.57	5.85	6.11	13.60	9.15	7.91	7.72	8.07
Sc	23.35	13.79	13.99	23.63	24.88	18.05	17.80	16.18	13.79	9.62	12.94	15.66	12.01
Sr	27.01	26.25	14.90	19.36	69.79	78.05	41.61	47.25	0.90	1.24	0.88	1.37	1.75
Ta	0.04	0.04	0.03	0.03	0.02	0.02	0.02	0.03	0.02	0.03	0.01	0.57	0.12
Th	0.10	0.08	0.06	0.09	0.02	0.62	0.01	0.13	0.05	0.11	0.06	0.06	0.13
U	0.11	0.02	0.03	0.15	0.07	0.12	0.02	0.25	0.15	0.07	0.03	0.03	0.10
V	121.62	92.74	95.39	154.78	124.32	89.80	92.87	85.72	89.57	71.06	89.54	69.75	87.78
Y	6.09	3.52	3.45	6.76	4.51	2.66	2.63	2.07	2.54	12.31	3.19	4.94	4.96
Zn	97.50	52.67	49.85	68.56	61.22	38.01	36.02	37.12	110.87	54.11	92.12	90.40	164.21
Zr	12.52	8.66	7.00	12.32	6.12	5.27	6.56	3.10	5.97	3.02	3.33	3.62	11.92
La	0.66	0.48	0.38	0.56	0.19	1.29	0.08	0.45	0.38	10.88	1.48	7.73	2.02
Ce	1.50	0.98	0.96	1.43	0.25	2.06	0.11	0.63	1.06	0.87	0.93	0.77	2.17
Pr	0.21	0.13	0.14	0.22	0.04	0.18	0.01	0.07	0.15	0.98	0.24	0.39	0.36
Nd	1.14	0.63	0.68	1.15	0.28	0.70	0.13	0.34	0.85	4.09	0.95	1.57	1.63
Sm	0.45	0.26	0.27	0.53	0.14	0.13	0.07	0.08	0.33	0.49	0.24	0.24	0.47
Eu	0.20	0.13	0.15	0.19	0.06	0.07	0.04	0.05	0.14	0.18	0.15	0.13	0.20
Gd	0.60	0.35	0.36	0.70	0.28	0.20	0.13	0.14	0.36	0.85	0.31	0.37	0.54
Tb	0.13	0.08	0.07	0.14	0.08	0.04	0.04	0.03	0.07	0.09	0.06	0.06	0.10
Dy	0.99	0.54	0.56	1.09	0.66	0.36	0.35	0.28	0.47	0.56	0.40	0.50	0.72
Ho	0.21	0.12	0.12	0.24	0.15	0.09	0.10	0.06	0.10	0.14	0.08	0.10	0.15
Er	0.59	0.33	0.35	0.68	0.45	0.26	0.29	0.21	0.27	0.32	0.22	0.26	0.43
Tm	0.09	0.05	0.06	0.11	0.07	0.04	0.05	0.04	0.04	0.03	0.03	0.04	0.06
Yb	0.60	0.35	0.35	0.71	0.47	0.27	0.33	0.23	0.25	0.16	0.19	0.24	0.38
Lu	0.09	0.05	0.05	0.11	0.08	0.04	0.05	0.03	0.04	0.02	0.03	0.04	0.06
Bi	0.20	0.19	0.14	0.25	0.016	0.016	0.015	0.017	0.033	0.021	0.031	0.03	0.051
Cd	0.06	0.07	0.07	0.07	0.036	0.029	0.071	0.034	0.034	0.065	0.055	0.043	0.047
Mo	0.07	0.06	0.06	0.09	0.031	0.056	0.156	0.063	0.116	0.064	0.389		
Sn	1.81	0.06	0.08	0.55		0.043		0.04	0.12	0.03	0.07	0.05	0.56

Table 1 (*continued*)

Sample	15MGEO-1A	15MGEO-1B	15MGEO-1C	15MGEO-1D	15MGEO-5A	15MGEO-5B	15MGEO-5C	15MGEO-5D	15MGEO-2A	15MGEO-2B	15MGEO-2C	15MGEO-2E	15MGEO-3
	Rio das Velhas greenstone belt												
Rock unit	Komatiite	Komatiite	Komatiite	Komatiite	Komatiite	Komatiite	Komatiite	Komatiite	High-Mg basalt	High-Mg basalt	High-Mg basalt	High-Mg basalt	High-Mg basalt
W	0.65	0.64	0.45	0.49	0.231	25.95	0.21	74.86	0.37	0.22	0.25	13.88	0.82
$(Al_2O_3/TiO_2)_{adj}$	30.44	27.64	28.19	29.26	47.47	43.13	41.49	38.36	13.61	18.25	10.90	11.75	11.17
$(CaO/Al_2O_3)_{adj}$	0.87	0.49	0.49	0.85	0.89	0.68	0.62	0.54	0.03	0.04	0.02	0.02	0.02
ΣREE	6.46	3.91	3.93	6.75	2.52	5.36	1.41	2.35	4.02	19.09	4.90	11.95	8.56
$(La/Sm)_{CN}$	0.91	1.16	0.88	0.66	0.83	6.37	0.74	3.64	0.74	13.98	3.89	19.94	2.67
$(Gd/Yb)_{CN}$	0.81	0.82	0.83	0.81	0.47	0.59	0.33	0.51	1.19	4.24	1.37	1.24	1.15
$(Gd/Yb)_{PM}$	0.83	0.84	0.84	0.82	0.48	0.61	0.33	0.52	1.22	4.34	1.40	1.27	1.17
$(Th/Nb)_{PM}$	1.92	1.82	1.70	2.38	1.63	2.27	1.63	0.51	1.86	2.28	2.78	0.61	2.20
$(Sm/Yb)_{PM}$	0.83	0.82	0.85	0.83	0.33	0.51	0.22	0.38	1.46	3.33	1.41	1.11	1.39
(La/Yb)PM	0.79	0.99	0.77	0.57	0.28	1.28	0.17	1.42	1.12	48.20	5.69	22.91	3.84
(Nb/Nb*)	0.90	1.04	0.98	0.49	0.33	1.78	0.29	4.81	0.66	0.07	0.16	0.20	0.25
(Ta/Ta*)	1.33	1.91	1.75	0.83	0.77	13.31	1.29	32.43	1.07	0.08	0.22	2.36	1.01
(Ti/Ti*)	0.83	0.95	0.88	0.84	1.18	1.45	1.88	2.03	0.75	0.11	0.52	0.59	0.96
(Eu/Eu*)	1.15	1.31	1.47	0.93	0.95	1.38	1.20	1.43	1.23	0.85	1.68	1.33	1.20
(Ce/Ce*)	0.98	0.95	1.03	1.01	0.69	0.92	0.84	0.79	1.10	0.05	0.35	0.07	0.58
(Zr/Th)	131.79	111.08	111.06	135.37	278.18	8.55	504.38	23.34	114.77	27.42	57.41	60.38	89.64
(Nb/Yb)	0.69	1.04	0.88	0.45	0.24	8.37	0.20	9.57	0.95	2.49	0.94	3.40	1.34
(Th/Yb)	0.16	0.23	0.18	0.13	0.05	2.26	0.04	0.59	0.21	0.68	0.31	0.25	0.35

Sample	PM14-01A	PM14-01B	PM14-01C	PM14-01D	PM14-08A	PM14-08B	PM14-08C	PM14-08D	PM14-10A	PM14-10B	PM14-10C	PM14-10D	PM14-11B	PM14-11C	PM14-12C
	Pitangui greenstone belt														
Rock unit	Basalt	Basalt	Basaltic anesite	Basalt	Basaltic anesite	Basalt	Basalt	Basaltic anesite	Gabbros	Gabbros	Gabbros	Gabbros	Basaltic anesite	Basalt	Basaltic anesite
Locality	Pitangui	Pitangui	Pitangui	Pitangui	Pitangui	Pitangui	Pitangui	Pitangui	Pitangui	Pitangui	Pitangui	Pitangui	Pitangui	Pitangui	Pitangui
Long. (°W):	44.93	44.93	44.93	44.93	44.9293	44.9293	44.9293	44.9293	44.8922	44.8922	44.8922	44.8922	44.9340	44.9340	44.9663
Lat. (°S):	19.41	19.41	19.41	19.41	19.6942	19.6942	19.6942	19.6942	19.7366	19.7366	19.7366	19.7366	19.6911	19.6911	19.6743
SiO_2	47.68	48.58	53.24	51	56.87	50.06	51.14	54.24	50.51	49.78	48.74	49.16	54.34	48.82	54.78
TiO_2	1.06	1.07	1.03	1.01	2.2	1.76	1.56	1.27	1.06	1.06	1.05	1.14	1.05	0.78	0.61
Al_2O_3	12.46	15.09	14.77	13.79	16.5	19.14	18.05	14.72	17.23	18.37	15.76	17.65	17.79	14.29	14.56
Fe_2O_3	16.13	15.61	12.19	14.38	11.77	14	14.05	17.52	8.38	7.68	9.34	8.59	11	8.21	8.48
MnO	0.28	0.23	0.2	0.23	0.14	0.24	0.18	0.12	0.12	0.11	0.12	0.13	0.19	0.22	0.14
MgO	6.5	5.66	4.81	6.01	4.46	6.39	6.59	4.59	6.77	6.99	9.37	6.61	5.06	3.01	8
CaO	11.55	9.04	8.8	8.47	0.63	0.38	0.37	0.68	10.69	10.78	11.06	11.76	1.71	11.67	7.13
Na_2O	1.72	2.69	3.46	2.75	0.6	0.7	0.25	0.96	2.7	2.73	2.26	2.11	5.18	1.81	2.79
K_2O	0.37	0.55	0.32	0.87	2.42	1.63	2.44	2.1	0.3	0.31	0.31	0.53	0.05	0.5	0.99
P_2O_5	0.12	0.14	0.13	0.14	0.34	0.26	0.21	0.19	0.24	0.25	0.2	0.25	0.11	0.08	0.08
LOI	1.93	1.17	0.91	1.19	3.84	5.18	4.97	3.41	1.71	1.71	1.54	1.83	3.32	10.4	2.23
Total	99.8	99.83	99.86	99.84	99.77	99.74	99.81	99.8	99.71	99.77	99.75	99.76	99.8	99.79	99.79
Adj Value															
$(SiO_2)_{adj}$	49.41	49.91	54.33	52.30	59.84	53.57	54.56	57.06	51.92	51.10	50.03	50.58	56.83	55.01	56.54
$(TiO_2)_{adj}$	1.10	1.10	1.05	1.04	2.31	1.88	1.66	1.34	1.09	1.09	1.08	1.17	1.10	0.88	0.63
$(Al_2O_3)_{adj}$	12.91	15.50	15.07	14.14	17.36	20.48	19.26	15.49	17.71	18.86	16.18	18.16	18.61	16.10	15.03
$(Fe_2O_3)_{adj}$	2.55	2.45	2.64	3.13	2.97	3.18	3.19	4.41	1.31	1.20	1.46	1.35	2.45	1.97	1.86
$(FeO)_{adj}$	12.75	12.23	8.81	10.45	8.48	10.61	10.62	12.61	6.57	6.01	7.31	6.74	8.15	6.56	6.20
$(MnO)_{adj}$	0.29	0.24	0.20	0.24	0.15	0.26	0.19	0.13	0.12	0.11	0.12	0.13	0.20	0.25	0.14
$(MgO)_{adj}$	6.74	5.81	4.91	6.16	4.69	6.84	7.03	4.83	6.96	7.18	9.62	6.80	5.29	3.39	8.26
$(CaO)_{adj}$	11.97	9.29	8.98	8.69	0.66	0.41	0.39	0.72	10.99	11.07	11.35	12.10	1.79	13.15	7.36
$(Na_2O)_{adj}$	1.78	2.76	3.53	2.82	0.63	0.75	0.27	1.01	2.78	2.80	2.32	2.17	5.42	2.04	2.88
$(K_2O)_{adj}$	0.38	0.57	0.33	0.89	2.55	1.74	2.60	2.21	0.31	0.32	0.32	0.55	0.05	0.56	1.02
$(P_2O_5)_{adj}$	0.12	0.14	0.13	0.14	0.36	0.28	0.22	0.20	0.25	0.26	0.21	0.26	0.12	0.09	0.08
Total	100	100	100	100	100	100	100	100	100	100	100	100	100	100	100
Ba	91.68	146.19	72.20	265.07	424.10	142.45	129.93	143.38	189.942	95.331	527	138	101.698	100.704	146.92
Be	0.46	0.51	0.58	0.48	0.45	0.51	0.62	0.45			0.27	0.24	0.36	0.24	0.26
Co	77.54	62.59	54.65	56.87	55.05	144.72	72.88	42.31			28.35	41.70	42.37	43.51	44.37
Cr	210.94	18.54	27.79	16.33	205.17	426.26	378.63	314.70	750	733	578.07	633.12	334.87	204.58	416.02
Cs	0.48	0.91	0.25	1.64	2.15	1.40	2.01	2.39			0.97	2.84	0.32	1.23	0.58
Cu															
Ga	15.23	15.70	15.19	13.98	19.40	20.49	17.26	14.48	14.7	14.2	13.39	15.14	13.82	11.66	9.51
Hf	2.55	2.73	2.63	2.56	4.21	4.11	3.60	3.06			1.23	1.29	1.88	1.40	1.19
Li	11.86	20.11	6.82	20.39	49.23	101.33	79.43	48.78			7.28	8.90	57.05	39.67	14.85
Nb	6.31	4.07	4.02	3.97	8.34	8.14	6.81	7.20	2.9	2.8	2.11	3.14	3.03	2.27	1.81
Ni	242.79	85.38	86.84	82.69	160.22	402.05	278.84	208.26	131	173	81.19	185.43	167.07	127.03	138.75
Pb	2.13	2.42	2.25	1.67	1.12	1.18	0.96	0.75	3.5	3.9	1.99	2.33	0.82	0.93	0.84
Rb	7.49	13.28	6.29	26.87	42.78	13.23	35.85	36.30	9.5	9.7	7.06	16.41	2.29	10.54	22.08
Sb	0.07	0.16	0.10	0.10	12.35	13.56	6.23	6.50			1.66	1.67	4.64	0.86	0.66
Sc	36.27	39.58	40.82	38.01	38.69	40.34	41.68	32.06	37	36	21.10	27.11	36.82	26.77	32.59
Sr	106.86	138.68	134.45	139.03	29.25	46.38	24.06	31.57	208	181	163.78	184.69	91.08	126.59	78.88
Ta	0.44	0.24	0.25	0.25	0.45	0.48	0.37	0.35			0.13	0.20	0.16	0.12	0.11
Th	1.16	1.17	1.10	1.08	0.92	0.78	0.82	0.65	2.3		0.36	0.40	0.33	0.21	0.50
U	0.31	0.32	0.28	0.28	0.40	0.23	0.36	0.45			0.16	0.19	0.14	0.49	0.15
V	243.12	262.68	290.06	250.01	310.70	302.21	300.69	246.63	218	242	181.92	229.80	219.90	169.58	207.72
Y	21.07	24.44	22.54	22.67	35.65	15.51	27.41	28.45	14	14.3	13.54	15.47	20.17	15.19	10.05
Zn	129.25	120.87	99.34	102.00	78.43	138.18	92.23	58.62	56	63	37.92	59.06	74.61	64.55	56.34
Zr	88.27	91.94	88.61	86.33	141.61	137.99	126.98	106.60	42	40	39.94	41.19	61.46	44.88	38.86
La	8.93	7.98	7.07	6.29	7.83	4.46	4.07	7.58			3.19	3.23	4.43	2.70	2.45

(*continued on next page*)

Table 1 (*continued*)

Sample	PM14-01A	PM14-01B	PM14-01C	PM14-01D	PM14-08A	PM14-08B	PM14-08C	PM14-08D	PM14-10A	PM14-10B	PM14-10C	PM14-10D	PM14-11B	PM14-11C	PM14-12C
	Pitangui greenstone belt														
Rock unit	Basalt	Basalt	Basaltic anesite	Basalt	Basaltic anesite	Basalt	Basalt	Basaltic anesite	Gabbros	Gabbros	Gabbros	Gabbros	Basaltic anesite	Basalt	Basaltic anesite
Locality	Pitangui	Pitangui	Pitangui	Pitangui	Pitangui	Pitangui	Pitangui	Pitangui	Pitangui	Pitangui	Pitangui	Pitangui	Pitangui	Pitangui	Pitangui
Ce	20.63	18.61	15.99	13.83	19.29	11.73	10.36	18.21	13	8	7.98	8.37	9.83	5.86	5.85
Pr	2.62	2.33	2.05	1.76	2.66	1.61	1.48	2.58			1.13	1.16	1.35	0.80	0.81
Nd	11.79	10.77	9.82	8.60	13.49	7.97	7.61	12.96	16	16	5.72	6.18	6.77	4.03	3.86
Sm	2.78	2.76	2.55	2.45	3.76	2.07	2.24	3.99			1.70	1.74	1.97	1.29	1.14
Eu	0.94	1.02	0.91	0.92	1.42	0.79	0.79	1.66			0.85	0.94	0.89	0.58	0.45
Gd	3.27	3.40	3.18	3.02	4.86	2.39	3.17	4.78			2.14	2.26	2.54	1.76	1.41
Tb	0.54	0.60	0.56	0.56	0.90	0.41	0.59	0.81			0.36	0.38	0.49	0.33	0.26
Dy	3.68	4.07	3.87	3.80	6.13	2.70	4.26	5.26			2.40	2.71	3.35	2.39	1.76
Ho	0.77	0.88	0.82	0.81	1.32	0.58	0.96	1.08			0.50	0.56	0.73	0.53	0.37
Er	2.23	2.56	2.38	2.39	3.87	1.88	2.98	2.96			1.42	1.62	2.12	1.58	1.06
Tm	0.33	0.38	0.35	0.36	0.58	0.31	0.45	0.44			0.21	0.24	0.32	0.23	0.16
Yb	2.06	2.38	2.16	2.28	3.57	2.03	2.72	2.72			1.22	1.48	1.90	1.54	0.94
Lu	0.33	0.41	0.35	0.38	0.60	0.37	0.44	0.45			0.20	0.24	0.31	0.27	0.16
Bi															
Cd															
Mo															
Sn	0.77	0.58	0.68	0.53	1.07	0.92	0.86	0.80				0.31	0.38	0.15	0.12
W	0.22	0.22	0.25	0.78	0.40	0.18	0.24	0.11			0.48	0.43	0.06	0.15	0.27
$(Al_2O_3/TiO_2)_{adj}$	11.75	14.10	14.34	13.65	7.50	10.88	11.57	11.59	16.25	17.33	15.01	15.48	16.94	18.32	23.87
$(CaO/Al_2O_3)_{adj}$	0.93	0.60	0.60	0.61	0.04	0.02	0.02	0.05	0.62	0.59	0.70	0.67	0.10	0.82	0.49
ΣREE	57.22	54.08	48.19	43.65	64.15	36.59	37.85	60.21			26.62	28.41	33.64	21.48	18.89
$(La/Sm)_{CN}$	2.00	1.80	1.73	1.60	1.30	1.35	1.13	1.19			1.17	1.16	1.41	1.30	1.34
$(Gd/Yb)_{CN}$	1.29	1.16	1.19	1.07	1.10	0.95	0.94	1.42			1.42	1.24	1.08	0.92	1.21
$(Gd/Yb)_{PM}$	1.32	1.18	1.22	1.09	1.13	0.97	0.96	1.45			1.45	1.27	1.11	0.94	1.24
$(Th/Nb)_{PM}$	1.54	2.42	2.29	2.29	0.93	0.80	1.01	0.75	6.65		1.42	1.06	0.90	0.78	2.31
$(Sm/Yb)_{PM}$	1.50	1.29	1.31	1.19	1.17	1.13	0.91	1.63			1.55	1.31	1.15	0.93	1.35
$(La/Yb)_{PM}$	3.11	2.41	2.35	1.98	1.57	1.58	1.07	2.00			1.88	1.57	1.68	1.26	1.87
(Nb/Nb*)	0.68	0.35	0.55	0.24	0.32	0.85	0.78	0.64			0.07	0.36	0.40	0.35	0.21
(Ta/Ta*)	0.81	0.36	0.58	0.26	0.30	0.87	0.73	0.54			0.08	0.41	0.36	0.31	0.21
(Ti/Ti*)	0.99	0.89	0.94	0.91	1.31	2.14	1.44	0.76			1.24	1.20	1.04	1.20	1.19
(Eu/Eu*)	0.95	1.02	0.97	1.03	1.01	1.08	0.90	1.17			1.36	1.45	1.22	1.17	1.08
(Ce/Ce*)	1.03	1.05	1.02	1.00	1.03	1.07	1.04	1.01			1.03	1.06	0.98	0.97	1.02
(Zr/Th)	76.10	78.31	80.70	79.71	153.42	176.91	154.10	165.28	18.26		111.57	103.75	188.52	213.70	78.18
(Nb/Yb)	3.07	1.71	1.86	1.74	2.33	4.01	2.51	2.65			1.73	2.13	1.60	1.47	1.92
(Th/Yb)	0.56	0.49	0.51	0.47	0.26	0.38	0.30	0.24			0.29	0.27	0.17	0.14	0.53

$Nb/Nb^* = 2^*Nb_{PM} / (Ba + La)_{PM}$.
$Ta/Ta^* = 2^*Ta_{PM} / (Ba + La)_{PM}$.
$Ti/Ti^* = Ti_{PM} / ((EU + Y)/2)_{PM}$.
$Eu/Eu^* = 2^*Eu_{PM} / (Sm + Gd)_{PM}$.
$Ce/Ce^* = 2^*Ce_{PM} / (La + Pr)_{PM}$.
$_{adj}$ = Adjusted value.
$_{PM}$ = Primitive mantle normalized value (taken from McDonough and Sun, 1995).
$_{CN}$ = Chondrite-normalized (taken from McDonough and Sun, 1995).

3. Sampling and petrography

For this study, we collected representative samples of komatiites and high-Mg basalts from the Rio das Velhas greenstone belt and basalts from the Pitangui greenstone belt (Table 1).

3.1. Komatiites: Rio das Velhas greenstone belt

Komatiites in the Rio das Velhas greenstone belt are restricted to the greenschist facies. Selected fresh komatiites were sampled from a single flow and a scattered unit near the Morro do Onça and Rio das Velhas (Table 1). The 0.5–1.5-m-thick komatiitic flow is composed of a spinifex layer. Random and oriented spinifex komatiites occur in the upper and lower parts of the spinifex layer, respectively. The principal minerals associated with komatiites are tremolite-actinolite, chlorite, albite, and serpentine (Fig. 2a–b).

3.2. High-Mg basalt: Rio das Velhas greenstone belt

Fresh high-Mg basalts were collected from the Nova Lima–Caeté and Santa Bárbara regions, which consist of fine-grained actinolite schists, occurring in pillowed and massive flows. The basalts contain plagioclase quartz, opaque minerals, albite, epidote, and chlorite.

3.3. Basalt: Pitangui greenstone belt

The Pitangui greenstone belt is predominantly formed by basalts and restricted gabbros. The basalts are dark and very fine- to fine-grained and form expansive flows. The foliation trend is predominantly NW-SE, dipping 20° to 80° NE–E. The Sn schistosity is the main structure. On outcrops, the pillowed basalts follow the Sn foliation, and, are mainly composed of plagioclase, actinolite, chlorite, talc, and quartz. Epidote, hornblende, clinozoisite, carbonate, opaque minerals, apatite, zircon, and titanite are accessory minerals (Fig. 2c).

The metagabbro occurs as an elongated pluton. It is grey to green, inequigranular, and coarse- to medium-grained. It has foliation of N15W to N10E, plunging between 50° and 85° NE–SE. The metagabbro is composed of hornblende, albite, augite, quartz, chlorite and talc. Accessory minerals are epidote, actinolite, clinozoisite, zircon, apatite, titanite, and opaque minerals (Fig. 2d).

4. Geochemical analytical procedures

4.1. Major and trace element analysis

For the analyses of the major elements and selected trace elements (Table 1), 1.2 g of the powdered sample were weighed and mixed with 6 g of lithium borate flux (comprising 35.3% tetraborate and

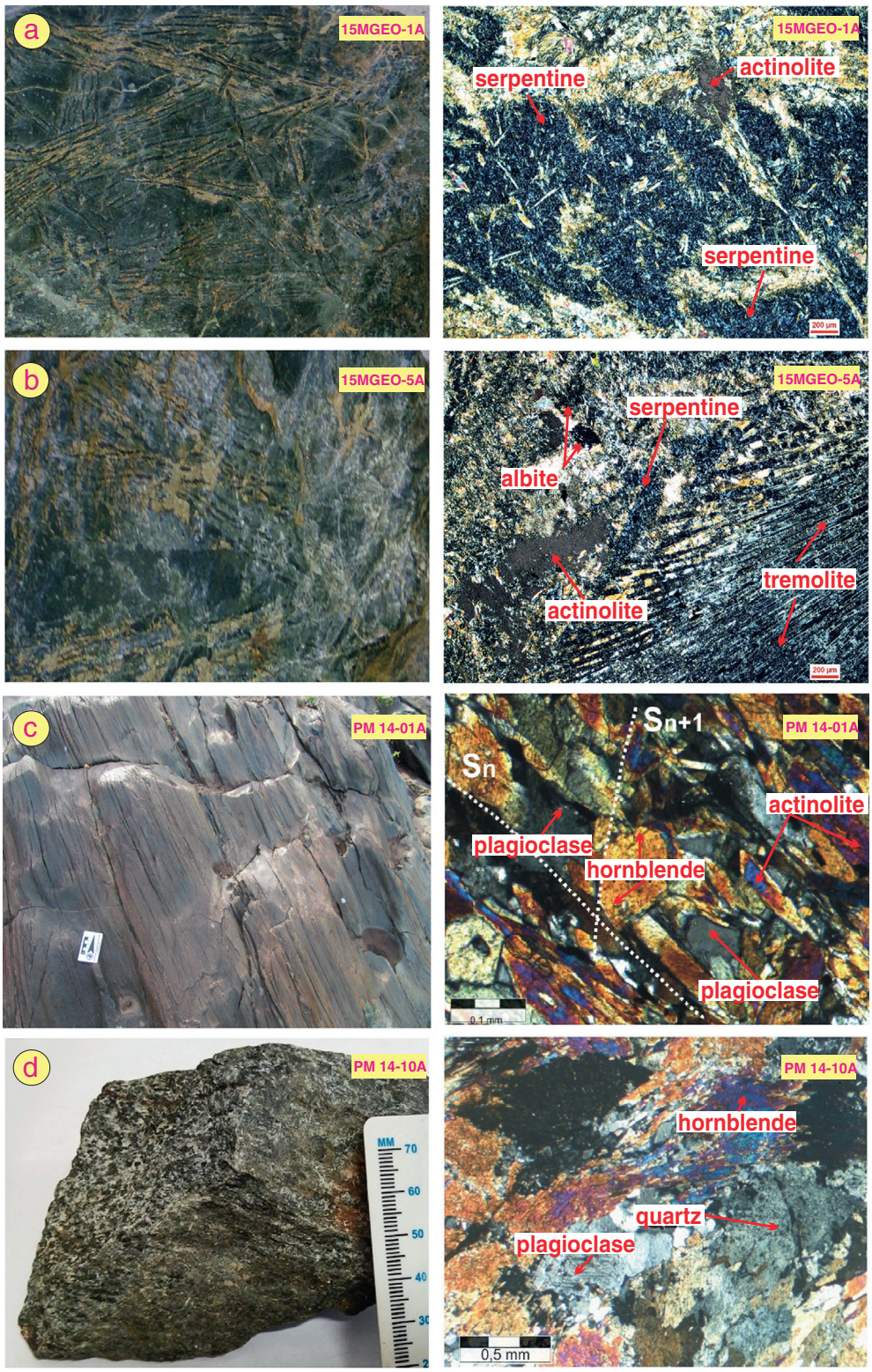

Fig. 2. (a–b) Occurrences and field and micro-photography of the Rio das Velhas komatiites (15MGEO-1A&5A) (spinifex texture) and mineral composition of tremolite-actinolite + chlorite + albite + serpentine; (c) field rock and micro-photograph of basalts (PM 14–01) from the Pitangui greenstone belt; (d) field rock and microphotograph of gabbros (PM 14-10A) from the Pitangui greenstone belt.

64.7% metaborate). The mixture was melted on a model M4-30 Claisse fusion system using a Pt–Au crucible at 1000 °C for ≈ approximately 8 min before being poured into a circular Pt mould and quenched in air to produce a flat disc. For trace element determinations, 9 g of sample powder was pressed into a pellet using 1.2 g of wax binding agent. The analyses of both the fused discs and pressed pellets were performed at the Institute of Geosciences, University of Campinas (UNICAMP) using a Philips PW 2100 X-ray fluorescence spectrometer. The analytical

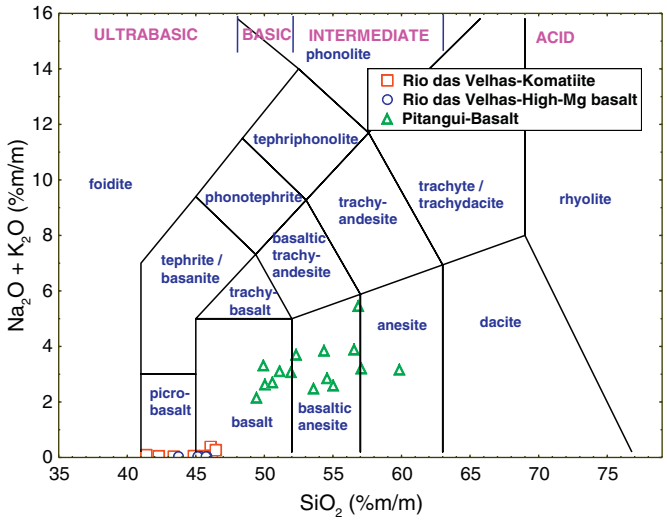

Fig. 3. Sample classification in the TAS diagram of Le Bas et al. (1986) obtained from the IgRoCS computer program (Verma and Rivera-Gómez, 2013) of the Rio das Velhas komatiites, high-Mg basalts and Pitangui basalts.

procedures were performed as described by Vendemiatto and Enzweiler (2001). Fe-oxidation adjustment followed the procedure of Middlemost (1989) on an anhydrous basis to 100%. This was easily achieved using the computer program, IgRoCS_M1 (Verma and Rivera-Gómez, 2013). Data quality was controlled routinely through analyses of the international reference rocks W-2 and BHVO for the major elements, and RGM-1 and WSE for the trace elements. The relative errors were 0.4–1.5% for the major and minor elements, and 1.5–10% for the trace elements.

The remaining rare earth and other trace elements were analysed on a quadrupole Thermo (Xseries2) ICP-MS at the Institute of Geosciences, University of Campinas. The analytical procedures were based on those of Eggins et al. (1997) and Liang et al. (2000). Cotta and Enzweiler (2009) described details of the instrument and sample preparation. The standards used for this work, were BRP-1, RGM-1 and GSP-2, with a 10% standard deviation.

5. Geochemical results

On the total alkalis vs. silica diagram (TAS; Le Bas et al., 1986; Fig. 3), the komatiites and high-Mg basalts plotted out mainly in the picro-basalt and basalt field, whereas the remaining nine samples plotted out in the basaltic andesite to andesite fields. These nine samples belonged to the Pitangui greenstone belt. According to the TAS diagram, the komatiites and high-Mg basalts were classified as komatiites because TAS can be used only for fresh rocks; therefore we used new multi-dimensional classification diagrams (Verma et al., 2016, 2017), that are based on altered-rock classifications. First, the samples were divided into common-Mg and high-Mg content groups (Fig. 4), then further plotted onto new multi-dimensional classification diagrams; the komatiites and high-Mg basalts were classified as komatiite and boninite respectively (Fig. 5a–d).

5.1. Whole-rock major and trace elements

5.1.1. Rio das Velhas komatiites

The analysed samples were komatiitic in composition with $(MgO)_{adj}$ content ranging from 28.61 wt.% to 38.54 wt.%. Similarly, the Ni (871–1989 ppm), and Cr (2799–4093 ppm) contents in the spinifex textured samples were high, but the $(TiO_2)_{adj}$ (0.15–0.235 wt.%) was low relative to other komatiites (Table 1; Dostal and Mueller, 2004). The Rio das Velhas komatiites have a narrow range of $(SiO_2)_{adj}$ content (41.39–46.4 wt.%). In Jenson's (1976) triangular diagram of $(Al_2O_{3adj}$-MgO_{adj}-$(Fe_2O_3 + TiO_2)_{adj}$, the komatiite samples plotted out in the komatiite field (Fig. 6). All eight komatiite samples were of the Al-undepleted Munro-type with $(CaO/Al_2O_3)_{adj}$ ratios between 0.49 and 0.89 and $(Al_2O_3/TiO_2)_{adj}$ ratios between 27.6 and 47.4.

5.1.2. Rio das Velhas high-Mg basalts

The high-Mg basalts were characterized by 43.7–45.7 wt.% $(SiO_2)_{adj}$, 39.5–41.5 wt.% $(MgO)_{adj}$, 0.83–2.6 wt.% $(Al_2O_3)_{adj}$, 0.83–2.6 wt.% $(TiO_2)_{adj}$, and 2552–2943 ppm Ni (Table 1). The $(Al_2O_3/TiO_2)_{adj}$ ratios (10.8–18.2) were similar to those of associated komatiites (Table 1). In Jenson's (1976) triangular diagram for $(Al_2O_{3adj}$-MgO_{adj}-$(Fe_2O_3 + TiO_2)_{adj})$, the high-Mg basalts plotted out in the komatiite field (Fig. 6).

5.1.3. Pitangui basalts

The basalts were characterized by 49.4–59.8 wt.% $(SiO_2)_{adj}$, 3.3–9.6 wt.% $(MgO)_{adj}$, 15.0–17.3 wt.% $(Al_2O_3)_{adj}$, 0.62–2.31 wt.% $(TiO_2)_{adj}$, and 81–402 ppm Ni (Table 1). The $(Al_2O_3/TiO_2)_{adj}$ ratios ranged from 7.5–23.8. In the triangular diagram of $(Al_2O_{3adj}$-MgO_{adj}-$(Fe_2O_3 + TiO_2)_{adj})$, these samples plotted out in the high-Fe tholeiite, high-Mg tholeiite, basalt, and andesitic fields (Fig. 6).

On the Fenner's binary diagrams of the major elements vs. $(MgO)_{adj}$, the majority of the major element oxides formed two clusters (komatiite and basalt) but together defined moderate trends for some of the major element oxides (Fig. 7). $(SiO_2)_{adj}$, $(TiO_2)_{adj}$, $(Al_2O_3)_{adj}$, $(Fe_2O_3)_{adj}$, $(CaO)_{adj}$, and $(P_2O_5)_{adj}$ exhibited moderate negative correlation with $(MgO)_{adj}$ whilst $(K_2O)_{adj}$ and $(Na_2O)_{adj}$ did not define any trend (see Fig. 7). For trace elements on the Fenner's diagrams, only Ni and Cr showed positive correlation with $(MgO)_{adj}$, whereas Ba, Yb, Y, Nd, and Zr showed moderate negative correlation (Fig. 8). Other trace element such as Rb showed scattering. The positive trends observed for Ni and Cr could be related to olivine fractionation, whereas the scattering of Rb could be due to post-magmatic alteration processes.

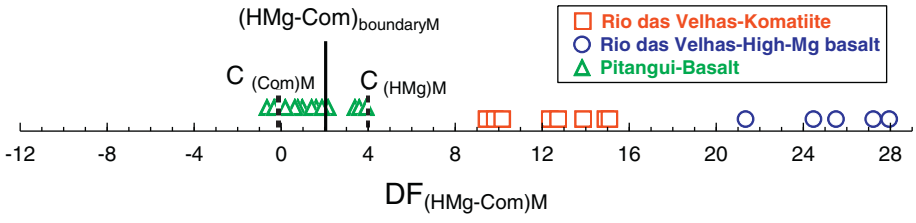

Fig. 4. Samples plotted in diagram based on discriminant function $DF_{(HMg\text{-}com)M}$ and Common (Com) rock subdivision based on major elements compositions (M); the classification field boundary $(HMg–Com)_{boundary}$ is shown for reference.

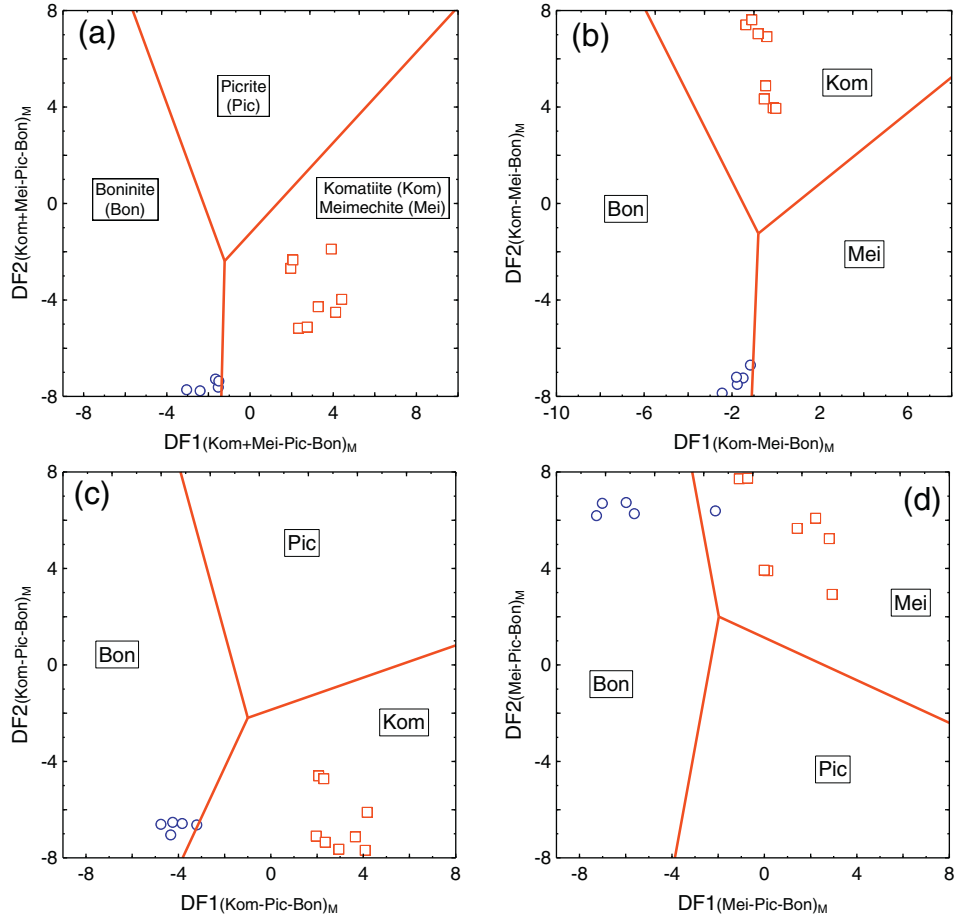

Fig. 5. a–d. Diagrams based on ilr-transformed major-elements (M) for achieving the subdivision of High-Mg rocks (1—komatiite; 2—meimechite; 3—picrate; 4—boninite, Verma et al., 2016).

5.2. Trace and rare earth element (REE) compositions

The trace element (including rare-earth element) compositions of the Rio das Velhas and Pitangui greenstone belts are presented in Table 1. A primitive mantle normalized (McDonough and Sun, 1995) multi-element diagram (Fig. 9a–c) showed a wide range in the concentration of the trace elements. In general, the Rio das Velhas komatiites and high-Mg basalts and the Pitangui basalts are enriched in highly incompatible LILE (e.g., Rb, Ba, U, Sr and LREE) relative to the moderately incompatible HFS elements (e.g., Nb, Ta, Th, and HREE). The normalized trace-element patterns are enriched in incompatible elements with negative Nb, Ta and Eu anomalies and a positive Zr anomaly (Fig. 9a–c) suggesting a subduction-related source.

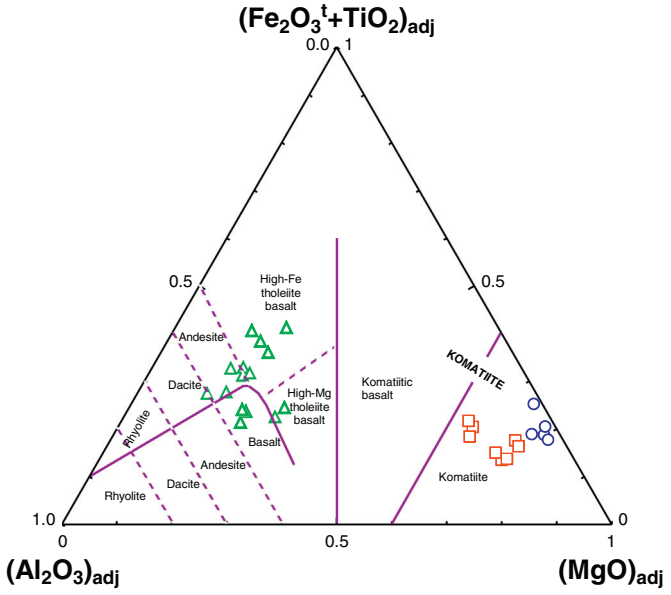

Fig. 6. Major elements (Al_2O_{3adj}-MgO_{adj}-$(Fe_2O_3 + TiO_2)_{adj}$) triangular plot. Modified after Jenson (1976).

Chondrite-normalized (McDonough and Sun, 1995) rare-earth element (REE) plots are shown in Fig. 10. The komatiites and high-Mg basalts showed little variation in their REE contents and exhibited a total REE content ranging from 1.40 to 6.75 ppm and 4.0 to 19.0 ppm, respectively. The Pitangui basalts displayed significant variation for REE but generally showed a higher total REE (18.9–64.1 ppm) compared to the komatiites and high-Mg basalts. The komatiite and high-Mg basalt samples displayed LREE-depleted (La/Sm_{cn} = 0.66–6.3) to enriched (La/Sm_{cn} = 0.70–13.9) patterns, whereas the basalts showed flat LREE patterns (La/Sm_{cn} = 1.13–2.00; Fig. 10). Both the komatiites and high-Mg basalts had moderately depleted (Gd/Yb_{cn} = 0.32–0.82) to flat (Gd/Yb_{cn} = 1.1–4.2) HREE patterns whereas basalts showed flat HREE patterns (Gd/Yb_{cn} = 1.0–1.4; Fig. 10). The komatiites and high-Mg basalts showed primitive geochemical characteristics. Zucchetti et al. (2000b) suggested that the rare-earth element patterns of the basalts and komatiites of the Rio das Velhas greenstone belts are similar to those of lavas derived from the partial melting of a mantle plume.

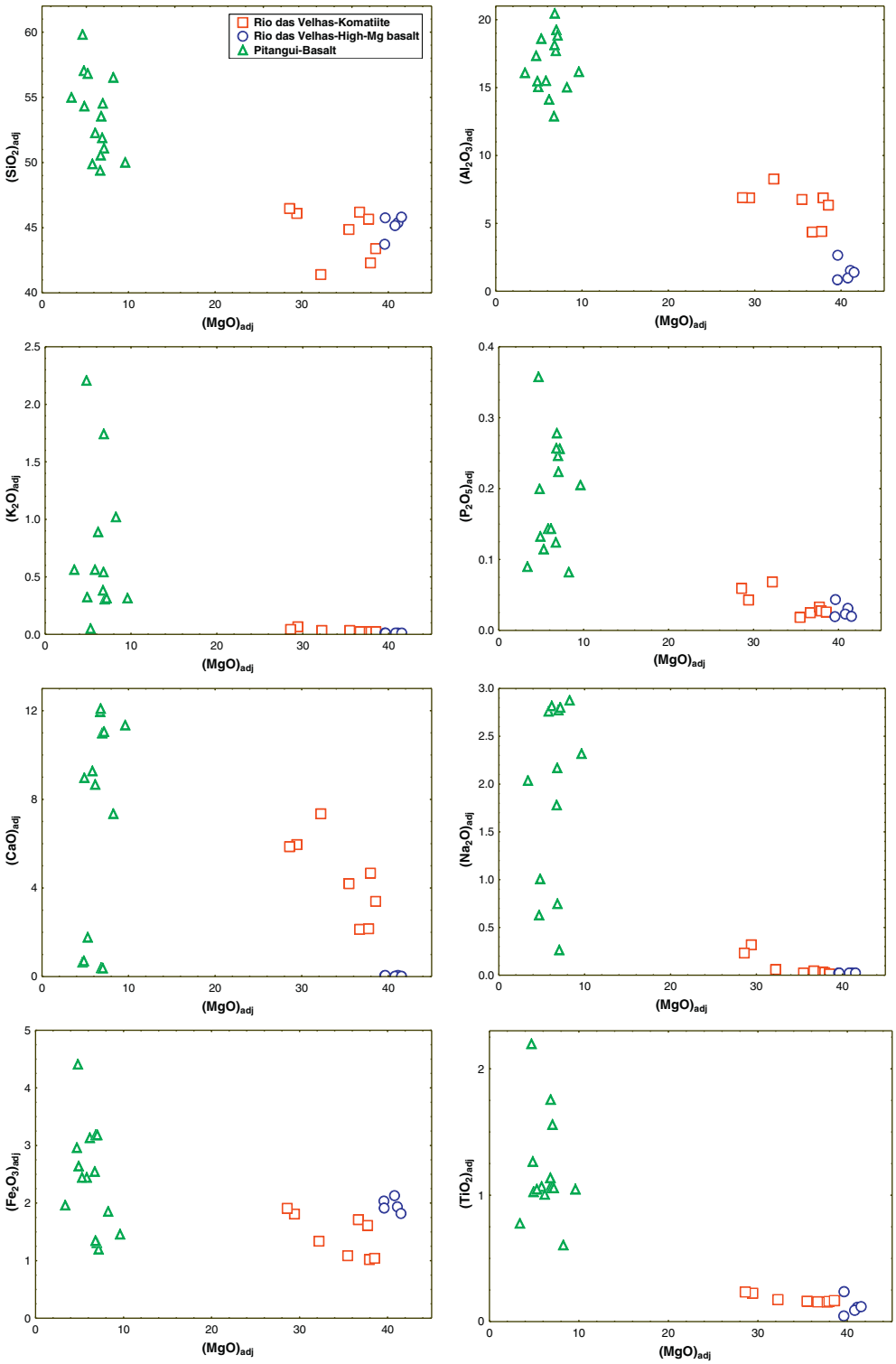

Fig. 7. Fenner's binary diagram showing moderate to strong fractionation trends for selected major elements oxide versus $(MgO)_{adj}$.

6. Discussion

6.1. Geochronology of the Rio das Velhas greenstone belt

The published ages of the Rio das Velhas greenstone belts are presented in Table 2. In this study, we discuss qualitatively the possible time frame of komatiite volcanism in the Rio das Velhas greenstone belt with respect to the timing of the surrounding TTG gneisses.

On the basis of U-Pb zircon ages Lana et al. (2013) suggested three magmatic events for the Quadrilátero Ferrífero area. The oldest TTG emplacement occurred during the Santa Barbara event ca. 3212–3210 Ma. The second event, named Rio das Velhas I, occurred from 2930–2900 Ma and was marked by the main magmatic additions of juvenile TTG rocks and the tectonic accretion of mafic–ultramafic greenstone belt terrains. The third event, Rio das Velhas II, from 2800–2770 Ma, is characterized by convergence-related felsic volcanic and plutonic rocks and the deposition of turbiditic wackes in the main greenstone belt sequence. Farina

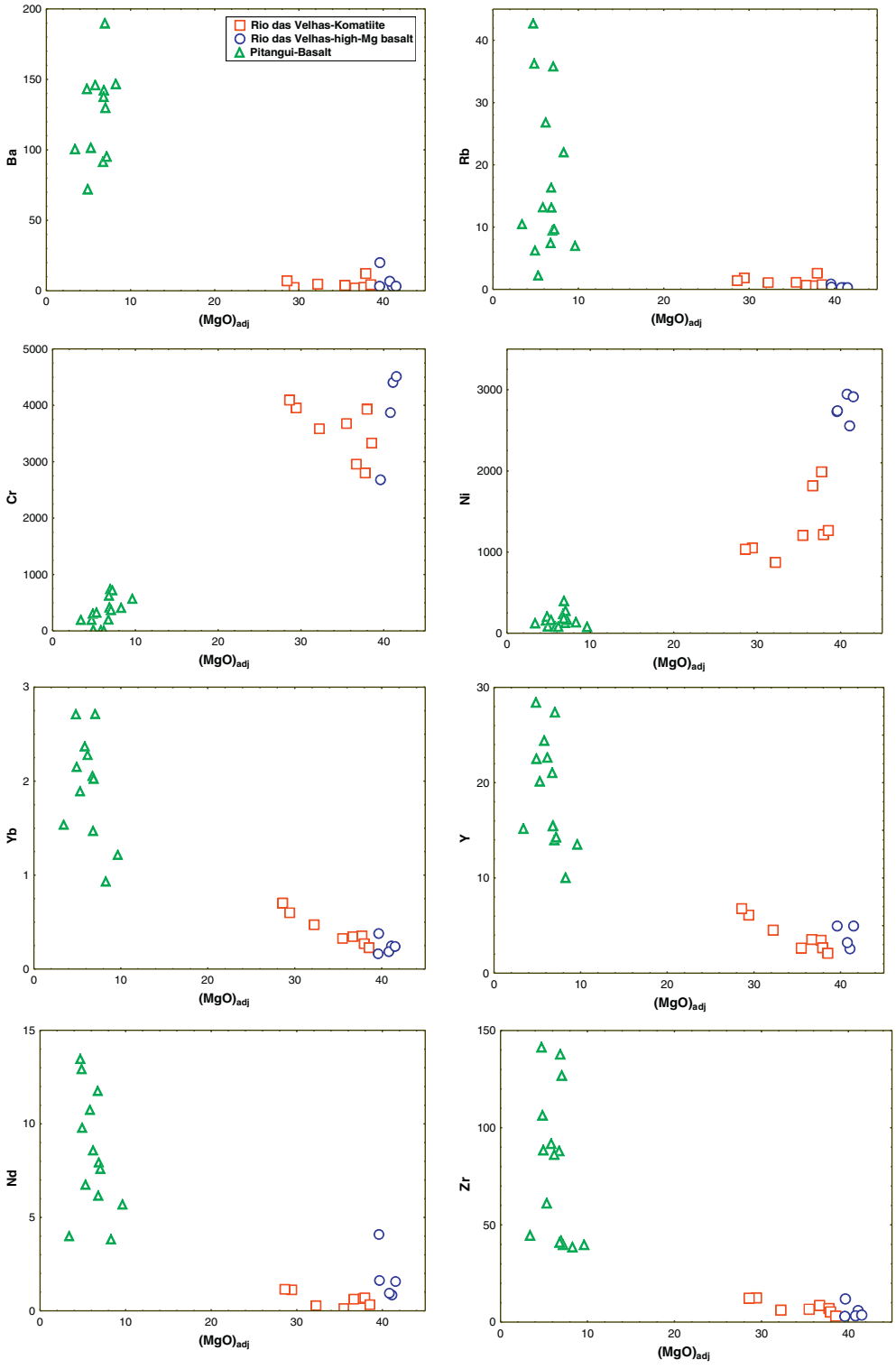

Fig. 8. Fenner's binary diagram showing correlation for selected trace elements versus $(MgO)_{adj}$.

et al. (2015) suggested a fourth magmatic event, named the Mamona event (2760–2680 Ma), during which numerous potassic granitoids were emplaced, leading to the cratonization of the region.

According to Lobato et al. (2001ab), a Sm–Nd isochron age of 2927 ± 180 Ma was reported for basaltic rocks from the Rio das Velhas greenstone belt. For volcanoclastic greywackes, Machado et al. (1992) and Noce et al. (2005) reported a U–Pb zircon age of 2792–2751 Ma. Similarly, a dacite flow intercalated within the sequence of mafic-to ultramafic volcanic rocks showed a zircon age of 2772 ± 6 Ma as reported by Machado et al. (1992). From the above evidences, we speculate that the komatiites and high-Mg basalts probably originated at 2790–2750 Ma or earlier, given that the Sm–Nd isochron technique is

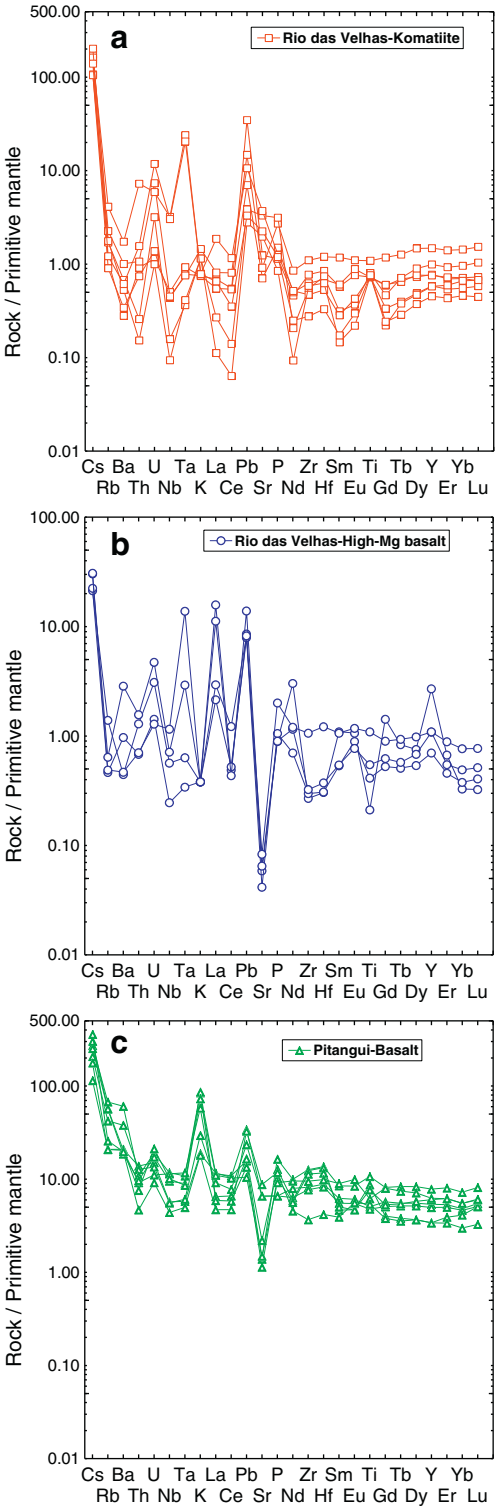

Fig. 9. a–c. Primitive mantle-normalized multi-element plots for the Rio das Velhas and Pitangui greenstone belts (McDonough and Sun, 1995).

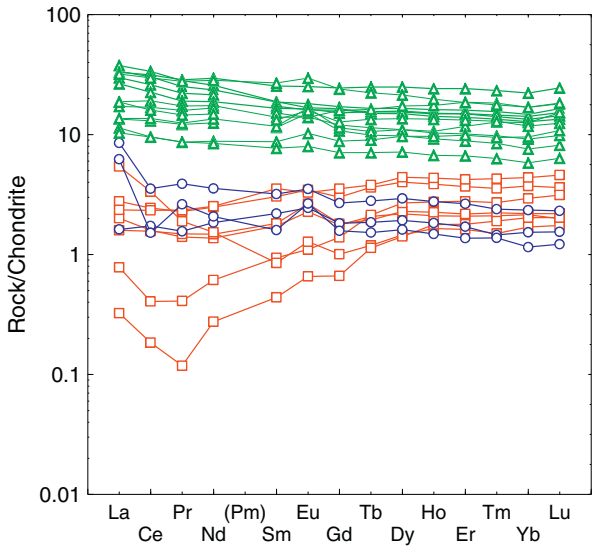

Fig. 10. Chondrite-normalized rare-earth element plots for the Rio das Velhas and Pitangui greenstone belts (McDonough and Sun, 1995).

not as robust as the U–Pb zircon technique and the above Sm–Nd age overlaps the error of the 2790–2750 Ma age interval. This suggestion implies an origin of the ultramafic to felsic volcanics during the Rio das Velhas II magmatic event, following the model proposed by Lana et al. (2013) for this event, which was marked by the emplacement of a felsic pluton and associated volcanic rocks in volcanic-arc systems developed around the margins of the 3220–2900 Ma continental block.

6.2. Geochronology of the Pitangui greenstone belt

Only few ages are available for this greenstone belt and the adjacent gneiss complex. As presented in Section 2, the ages for the greenstone belt (Silva, 2016; Silva et al. under review) are 2771 ± 18 Ma for the metabasalt, 2740 ± 36 Ma for the metagabbro, and 2876 Ma for the gneiss from the Divinópolis complex. Detrital zircon grains from the clastic sedimentary rocks show a maximum depositional age of 2720 Ma, or possibly 2670 Ma (Silva, 2016; Silva et al. under review) or 2859 Ma (Soares et al., 2017). If we correlate these data with the main magmatic events in the Quadrilatero Ferrífero area (Lana et al., 2013), the Pitangui basalts are coeval with the Rio das Velhas II magmatic event and the metagabbro was emplaced later during the Mamona event.

6.3. Degree of post-magmatic alteration

Geochemical and isotopic studies of Archean komatiites across the world have revealed that the mobility of LILE and REE in most cases is controlled by secondary processes, such as metamorphism or hydrothermal alteration (Arndt et al., 1989; Chavagnac, 2004; Gruau et al., 1992; Lesher and Stone, 1996). The mobility of LILE persists without affecting the abundances of HFSE, HREE, Zr, and Hf (Arndt, 1986; Lesher and Stone, 1996). Silica mobility shows a negative correlation between $(SiO_2)_{adj}$ and $(MgO)_{adj}$ (Fig. 7), although it is possible that the komatiite samples may have lost silica due to serpentinization, and therefore fall below the olivine fractionation line (Fig. 11). Thus, the preserved mineralogy (e.g., serpentine) indicates recrystallization under low-grade conditions. In this study, we used immobile elements (HFSE and REE) for the interpretation of petrogenetic processes. The chondrite-normalized diagram showed a flat REE pattern, whereas the primitive mantle-normalized diagram indicated zigzag patterns of LILE due to alteration and mobility. Furthermore, the major elements, such as $[(Al_2O_3)_{adj}, (CaO)_{adj}, (TiO_2)_{adj}$ and $(P_2O_5)_{adj}]$ showed smooth fractionated trends with MgO (Fig. 7), which suggests that there was no major alteration of the komatiites. Interpretation of the immobile elements (HFSE and REE) showed that there were no significant secondary alteration processes. The komatiites and high-Mg basalts showed negative Ce anomalies (see Figs. 9–10), whereas the basalts showed positive Ce anomaly. According to Braun et al. (1993), the Ce anomalies are

Table 2
Published geochronology of the greenstone belt of Rio das Velhas.

SL. No.	Greenstone belt	Rock	Method	Age	References
1	Rio das Velhas	Volcanic	TIMS	2776 ± 26 Ma	Machado et al. (1992)
2	Rio das Velhas	Volcanic	SHRIMP	2792 ± 11 Ma	Noce et al. (2005)
3	Rio das Velhas	Volcanic	TIMS	2751 ± 11 Ma	Noce et al. (2005)
4	Rio das Velhas	Volcanic	TIMS	2777 ± 7 Ma	Noce et al. (2005)

produced by different oxidation states such as Ce^{3+} and Ce^{4+}. Once Ce^{4+} reacts with water, it precipitates in the form of CeO_2. The depletion of Ce and the resulting negative Ce anomalies could be attributed to the removal of Ce by circulating fluids during metamorphism. This process indicates that the Rio das Velhas greenstone belt komatiites may have experienced alteration during greenschist facies metamorphism. In some greenstone belts, Eu anomalies have been used to discover hydrothermal secondary alteration processes (Arndt, 1994; Lécuyer et al., 1994; Ludden et al., 1982). In summary, the studied komatiites and high-Mg basalts were not affected by large-scale alteration processes. Thus, the geochemical data of these rocks can be used to constrain the Archean mantle.

6.4. Crustal contamination

Mantle-derived magma can be contaminated by crustal material either by the assimilation of wall rock or the thermal erosion of continental lithosphere. Incompatible element ratios (i.e., between LREE and HFSE) are suitable indicators for evaluating crustal contamination, because these ratios are enriched in continental crust compared to the mantle. Field relationships and stratigraphy reveal that the Rio das Velhas komatiites are associated with pillowed basalts and a submarine environment (Zucchetti et al., 2000a, 2000b). Furthermore, the negative Nb anomalies could reflect mantle either source characteristics or crustal contamination during magma emplacement, whereas the studied komatiites did not indicate LREE enrichment, thus showing mantle inheritance. Except for two samples that had low Zr/Th ratios of 8.5 and 23.3, the Zr/Th ratio in our samples had a range of 111–504, which is similar to or higher than the primitive mantle value of 116 (Fan and Kerrich, 1997). The Zr/Th ratio of the continental crust is ~20, which precludes crustal contamination for the Rio das Velhas komatiites, high-Mg basalts and the Pitangui basalts. These results are also supported by the Th/U, La/Sm, Nb/Y, and Zr/Nb ratios, because the ratio value for most of the samples was close to the recommended values for Archean primitive mantle (Campbell, 2002; Condie, 2003). Finally, the bi-variate diagram of Pearce (2008), which is based on petrogenetic modelling of immobile trace elements (Nb–Yb vs Th–Yb), did not show any crustal contamination (Fig. 12a–b).

6.5. Mantle source composition

Geochemical ratios such as [$(CaO/Al_2O_3)_{adj}$, $(Al_2O_3/TiO_2)_{adj}$ and $(Gd/Yb)_{PM}$] are most useful for evaluating mantle source characteristics in

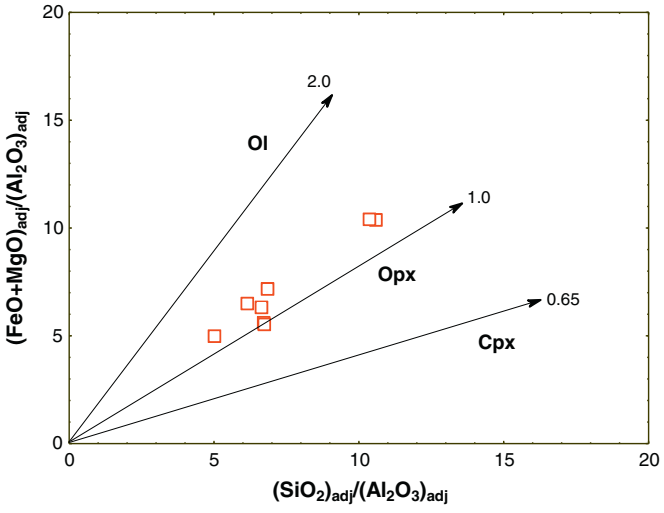

Fig. 11. Bivariate $(SiO_2/Al_2O_3)_{adj}$ versus $(FeO + MgO)_{adj}/Al_2O_3)_{adj}$ diagram of Pearce (1968) for Rio das Velhas komatiites. Arrows indicate lines for olivine, orthopyroxene and clinopyroxene.

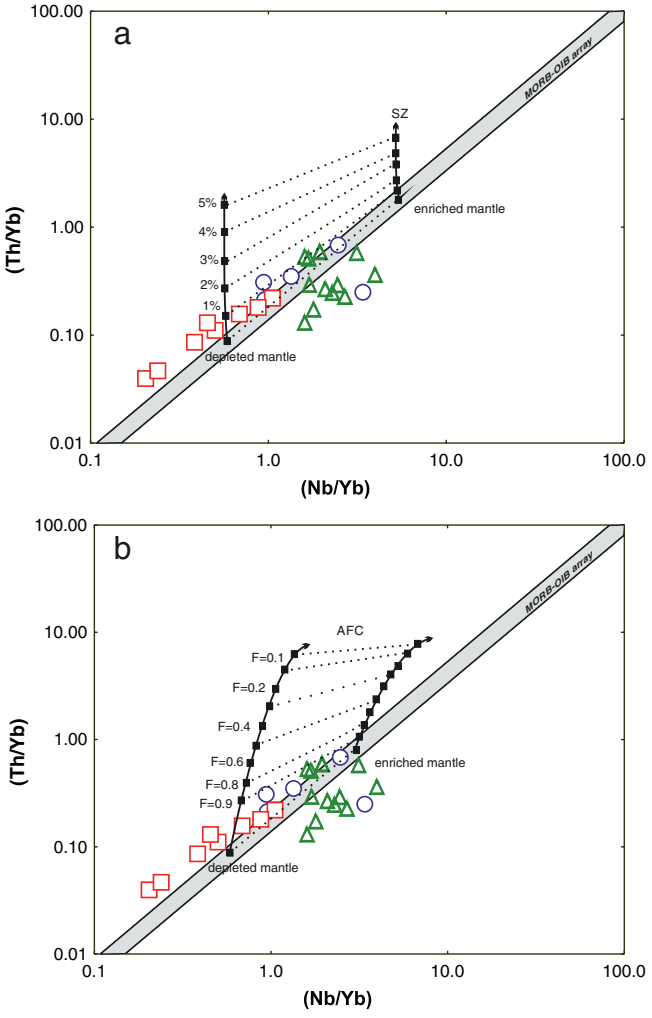

Fig. 12. a–b. Petrogenetic modelling of the Th/Yb–Nb/Yb projection after Pearce (2008). A) subduction zone enrichment of depleted and enriched mantle wedges by fluids, with percentages of subduction component in wedge; note that enrichment is higher in depleted mantle wedges; B) crustal contamination of depleted and enriched magmas with the continental crust; F denotes percentage of magma left.

terms of the fractionation or retention of garnet in the mantle residue (Chavagnac, 2004; Jahn et al., 1982). Archean komatiites are divided into two types: Al-depleted and Al-undepleted (e.g., Arndt and Nisbet, 1982; Fan and Kerrich, 1997; Sproule et al., 2002). Furthermore, Arndt (2003) classified komatiites as Al-depleted Barberton-type and Al-undepleted Munro-type. Al-depleted or Barberton type komatiites are characterized by sub-chondritic ratios [$(Al_2O_3/TiO_2)_{adj} \leq 16$] and [$(CaO/Al_2O_3)_{adj} > 1.0$], flat REE patterns with enriched incompatible elements, and a high [$(Gd/Yb)_{PM} > 1.0$] value. Conversely, Al-undepleted or Munro type komatiites are characterized by near chondritic ratios [$(Al_2O_3/TiO_2)_{adj} > 20$] and [$(CaO/Al_2O_3)_{adj} \leq 1.0$], relatively low abundances of incompatible elements, the depletion of light rare earth elements (LREE) and non-fractionated heavy rare earth elements (HREE) patterns and a low [$(Gd/Yb)_{PM} \leq 1.0$]. In this study, the Rio das Velhas komatiites were classified as Al-undepleted komatiites due to an $(Al_2O_3/TiO_2)_{adj}$ ratio ranging from 27–47 and a $(CaO/Al_2O_3)_{adj}$ ratio ranging from 0.48–0.89, which suggest that garnet entered into the melt phase during partial melting of the mantle. The low $(La/Yb)_{PM}$, $(Th/Nb)_{PM}$, and $(Sm/Yb)_{PM}$ ratios (0.16–1.41, 0.51–2.37, and 0.22–0.84, respectively) support a high degree of mantle melting. The low $(TiO_2)_{adj}$ contents also corroborate this hypothesis. Fig. 13(a–b) shows binary plots of $[(Al_2O_3/TiO_2)_{adj}$ vs $(Gd/Yb)_{PM}$ and $[(CaO/Al_2O_3)_{adj}$ vs $(Gd/Yb)_{PM}]$ for garnet partial melts using data from this study.

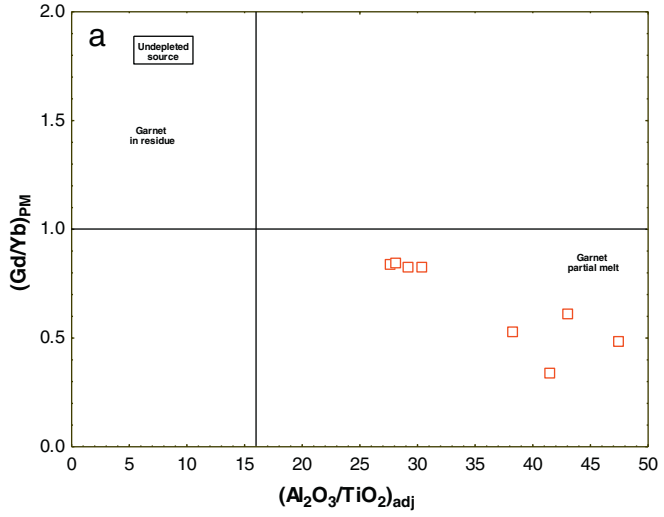

Fig. 13. a–b. Bivariate plot of $[(Al_2O_3/TiO_2)_{adj}$ versus $(Gd/Yb)_{PM}]$ ratios and $[(CaO/Al_2O_3)_{adj}$ versus $(Gd/Yb)_{PM}]$ ratio for Rio das Velhas komatiites.

6.6. Temperature and melting processes of komatiite magmas

Komatiitic rocks have a very high melting point of more than 1600 °C. Hanson and Langmuir (1978) modelled the partial melting of mantle pyrolite at 1 atmosphere of pressure. They used the model equation of Roeder and Emslie (1970) for the partitioning of magnesium and iron between olivine and melt and calculated the abundances of $(MgO)_{adj}$ and $(FeO)_{adj}$ in the resultant melts and residual solids. The $(MgO\text{-}FeO)_{adj}$ diagram shows fields of melts and of residual solids, both contoured for the percentage of partial melting and associated temperatures (Fig. 14). Olivine fractional crystallization trends in melts of differing composition are superimposed on the melt field. Furthermore, we plotted komatiites, high-Mg basalts, and basalts on bivariate diagrams of $(MgO)_{adj}$ vs $(FeO)_{adj}$. The komatiites and high-Mg basalts plotted out in the field of liquidus that probably co-existed with mantle peridotite, whereas the basalts were plotted out outside the liquidus field, due to differences between the equilibrium and fractional crystallization of olivine (Fig. 13). The komatiites corroborate a high degree (>30%) of mantle melting with a liquidus temperature of 1500 °C. Therefore, the komatiites and basalts were derived from the mantle at different temperatures and depths.

6.7. Tectonic setting discrimination

In this study, we used new multi-dimensional discrimination diagrams to infer the plate tectonic setting, because conventional bivariate and ternary diagrams for tectonic discrimination were shown to work unsatisfactory (Verma, 2010). The most important reasons for this failure are related to the use of limited databases, the problem of closed or constant sum compositional variables, and eye-fitted tectonic field boundaries and distribution of compositional data (Armstrong-Altrin, 2015; Verma, 2015; Verma and Armstrong-Altrin, 2016; Verma et al., 2012, 2013, 2015a, 2015b). Therefore, the new multi-dimensional discrimination diagrams proposed by Verma et al. (2006), Verma and Agrawal (2011) and Verma and Verma (2013), which are based on log-ratio transformation and linear discriminant analysis, have been used to understand tectonic regime dominant for magma genesis. The set of two diagrams by Verma et al. (2006) requires the availability of a complete data set of all major elements (Fig. 15a–b). These diagrams have four tectonic settings and can discriminate between basic and

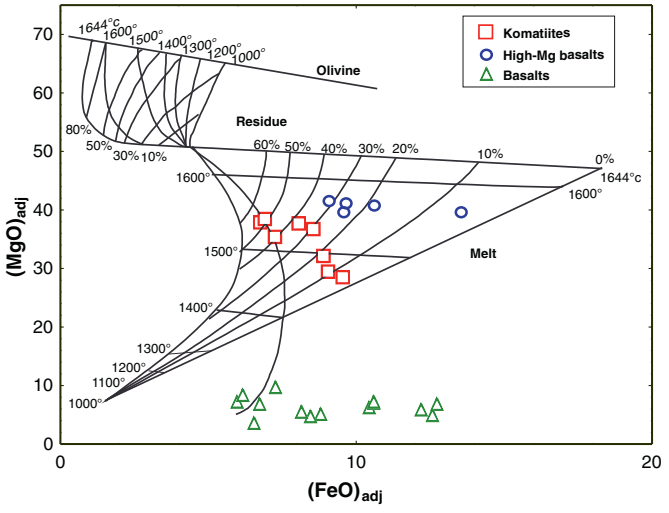

Fig. 14. Field of partial melts and residue, calibrated in liquidus temperature plotted on a $(FeO)_{adj}$–$(MgO)_{adj}$ (wt.%) diagram for the Rio das Velhas komatiite, high-Mg basalts and Pitangui basalts (after Hanson and Langmuir, 1978).

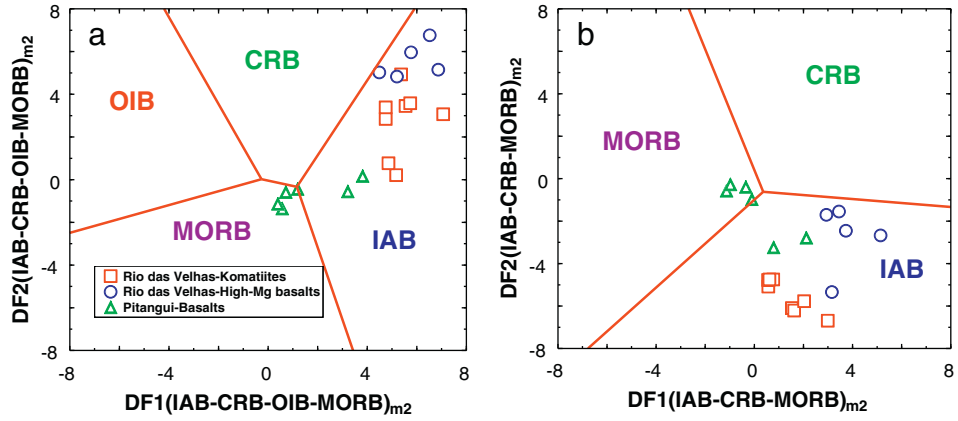

Fig. 15. a–b. Application of the set of two log–ratio transformed major element–based discriminant function DF1–DF2 discrimination diagrams (see the subscript m2 in all these diagrams; Verma et al., 2006) for basic rock samples from Rio das Velhas and Pitangui greenstone belts, Brazil. The four fields that can be discriminated are: IAB–island (and continental) arc basic rocks; CRB–continental rift basic rocks; OIB–ocean island basic rocks; MORB–mid-ocean ridge basic rocks.

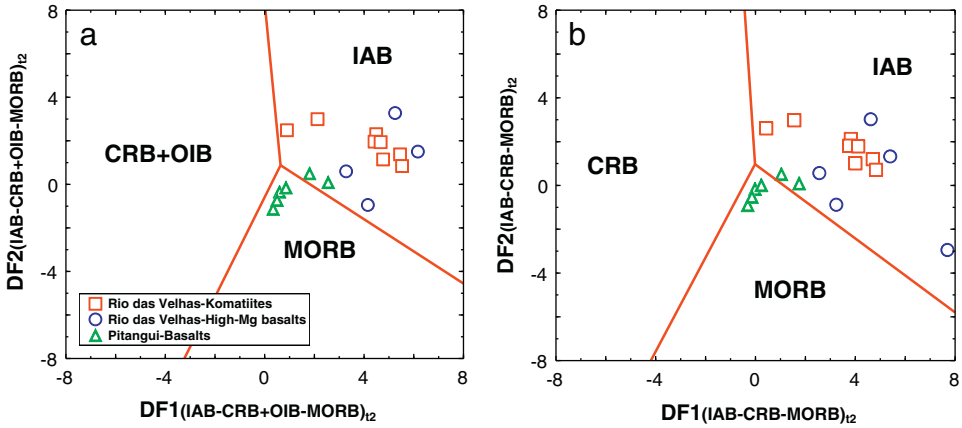

Fig. 16. a–b. Application of the set of two log–ratio transformed immobile trace element–based discriminant function DF1–DF2 discrimination diagrams (see the subscript t2 in all these diagrams; Verma and Agrawal, 2011) for basic rock samples from Rio das Velhas and Pitangui greenstone belts, Brazil.

Table 3
Application of multidimensional diagrams to Neoarchean (2700 Ma) intermediate rocks of the Pitangui greenstone belt.

Magma type, Figure name	Figure type	Total number of samples	Number of discriminated samples				
			Arc			CR + OI [x ± s] [p_CR + OI] Θ	Col [x ± s] [p_Col] Θ
			IA + CA [x ± s] [p_IA + CA] Θ	IA [x ± s] [p_IA] Θ	CA [x ± s] [p_CA] Θ		
Intermediate; Verma and Verma (2013); log-ratios of immobile trace elements	(IA + CA-CR + OI-Col)	9	6 [0.861 ± 0.103] (0.6929–0.9313)	–	–	3 [0.589 ± 0.059] (0.5289–0.6474)	0 (0)
	(IA-CA-CR + OI)	9	–	9 [0.780 ± 0.136] (0.4381–0.8812)	0 (0)	0 (0)	–
	(IA-CA-Col)	9	–	8 [0.814 ± 0.083] (0.6734–0.9587)	1(0.5263)	–	0 (0)
	(IA-CR + OI-Col)	9	–	8 [0.881 ± 0.068] (0.7822–0.9544)	–	1(0.5297)	0 (0)
	(CA-CR + OI-Col)	9	–	–	7 [0.800 ± 0.168] (0.5396–0.9496)	2 [0.724 ± 0.081] (0.6665, 0.7816)	0 (0)
Diagrams based on log-ratios of immobile trace elements	{Σn} {Σprob} [%prob]	45	{6} {5.1685} [−--]	{25} {20.5840} [69%]	{8} {6.1232} [21%]	{6} {3.7458} [10%]	{0} {0} [0%]

IA—island arc; CA—continental arc; IA + CA—combined island and continental arcs, i.e., arc setting; CR—continental rift; OI—ocean island; CR + OI—combined continental rift and ocean island, i.e., within-plate (WP) setting; Col—collision; Θ the probability values for samples from a given locality are represented by (pIA + CA)—probability for the combined island and continental arc setting in the first diagram; [pIA]—probability for the island arc setting in the diagrams; [pCA]—probability for the continental arc setting in the diagrams; [pCR + OI]—probability for the combined continental rift and ocean island setting in all diagrams; [pCol]—probability for the collision setting in the diagrams; − mean ± 1SD (standard deviation) of the probability estimates for all samples discriminated in a given tectonic setting; these are reported in []; the final rows give a synthesis of results as {Σn} {Σprob} [%prob], where {Σn} is the total number of samples or data points plotting in all five diagrams is reported in the column of total number of samples, whereas the sum of samples plotting in a given tectonic field is reported in the respective tectonic field column; {Σprob} is the sum of probability values for all samples plotting in a given tectonic field is reported in the respective tectonic field column; and [%prob] is the total probability of a given tectonic setting expressed in percent after assigning the probability of IA + CA to IA and CA (using weighing factors explained in Verma and Verma, 2013).

ultrabasic magmas. The other set by Verma and Agrawal (2011) is based on the availability of concentration data for the so-called relatively immobile elements (Nb, V, Y, Zr, and $(TiO_2)_{adj}$; Fig. 16 a–b). Similarly, for intermediate rock diagrams, the first five diagrams are based on immobile major and trace elements $(MgO)_{adj}$, $(TiO_2)_{adj}$, $(P_2O_5)_{adj}$, Nb, Ni, V, Y, and Zr, whereas the other set, by Verma and Verma (2013), is based on immobile trace elements (La, Yb, Ce, Sm, Nb, Th, Y, and Zr; Table 3).

In the new multi-dimensional discrimination diagrams by Verma et al. (2006) the komatiite and high-Mg basalt samples from the Rio das Velhas greenstone belt were discriminated as an IAB setting, whereas the Pitangui greenstone belt basalts were discriminated as a MORB setting (Fig. 15a–b). Simultaneously, we used immobile major-trace element based discrimination diagrams (Verma and Agrawal, 2011) and most of the samples were also plotted in an IAB setting for the Rio das Velhas komatiites and high-Mg basalts, and a MORB setting for the Pitangui (Fig. 16a–b). Finally, nine samples of Pitangui basalts of intermediate composition indicated an IA setting (Table 3). We clarify that the intermediate rocks were discriminated as island arc (IA), continental arc (CA), within-plate (CR + OI), and collision tectonic settings, because one tectonic setting is missing from these sets (e.g., MORB from the intermediate diagrams and Col from the basic diagrams). Therefore, the Rio das Velhas komatiites and high-Mg basalts were probably generated in an IA setting or a subduction-related setting, whereas the Pitangui basalts indicate a MORB to IA setting (Verma and Agrawal, 2011). The negative Nb and Ta anomalies in the primitive mantle-normalized multi-element diagrams for the Rio das Velhas and Pitangui greenstone belts also support these findings. In some island arc settings, komatiites and high-Mg basalts were probably extruded in the fore-arc region (Parman and Grove, 2004).

7. Conclusions

The main outcomes of the study can be summarized as follows:

1. The Rio das Velhas greenstone belt is composed mainly of komatiites and high-Mg basalts, whereas the Pitangui greenstone belt is composed of normal basalts.
2. Major- and trace-element ratios such as $[(CaO/Al_2O_3)_{adj}$, $(Al_2O3/TiO_2)_{adj}$ and $(Gd/Yb)_{PM}]$ indicate that the Rio das Velhas komatiites are similar to Al-undepleted Munro-type komatiites.
3. The Rio das Velhas komatiites and high-Mg basalts were derived from partial melting of the mantle at different depths with the influence of garnet in the melt phase. The spinifex structure reveals very high eruption temperatures (~1450–1550 °C) for these komatiites and high-Mg basalts.
4. Trace-element data, particularly incompatible element contents suggest that the komatiites, high-Mg basalts, and basalts were derived from depleted mantle.
5. The studied komatiites, high-Mg basalts and basalts were not affected by large-scale alteration processes. Thus, the geochemical data of these rocks can be used to constrain Archean mantle composition and processes.
6. New multi-dimensional discrimination diagrams and conventional multi-element normalized diagrams suggest a subduction-related—especially island-arc—tectonic setting for the Rio das Velhas komatiites and high-Mg basalts. A MORB to IA setting is suggested for the Pitangui greenstone belt because the MORB setting is absent from the intermediate rock diagrams.

Acknowledgements

This research was funded by The São Paulo Research Foundation (FAPESP) thematic project “Evolution of Archaean Terranes of the São Francisco Craton and the Borborema Province, Brazil: global environmental and geodynamic implications” [grant # 2012/15824-6 awarded to EPO] and postdoc grants to SKV [2012/07243-3] and JAM [2014/04920–0]. EPO and WSA also acknowledge the Brazilian National Research Council (CNPq) for research grant [# 305658/2015-8 and # 312509/2014-6, respectively]. We are highly grateful to Prof. Vinod K. Singh and anonymous reviewer for their constructive comments, which helped us to improve our presentation. We also thank Editor-in-Chief Prof. Nelson Eby for his editorial handling and guidance.

References

Abbott, D., Burgess, L., Longhi, J., Smith, W.H.F., 1994. An empirical thermal history of the Earth's upper mantle. Journal of Geophysical Research - Solid Earth 99, 13835–13850.
Alkmim, F.F., Teixeira, W., 2017. The Paleoproterozoic Mineiro Belt and the Quadrilátero Ferrífero. In: Heilbron, M., Cordani, U.G., Alkmim, F.F. (Eds.), São Francisco Craton, Eastern Brazil. Tectonic Genealogy of a Miniature Continent. Regional Geology Series. Springer International:pp. 71–94. http://dx.doi.org/10.1007/978–3–319-01715-0_5.
Alkmim, F.F., Marshak, S., Fonseca, M.A., 2001. Assembling West Gondwana in the Neoproterozoic: clues from the São Francisco craton region, Brazil. Geology 29, 319–322.
Almeida, F.F.M., 1977. O cráton do São Francisco. Revista Brasileira de Geociencias 7, 349–364.
Almeida, F.F.M., Hasui, Y., de Brito Neves, B.B., Fuck, R.A., 1981. Brazilian structural provinces: an introduction. Earth Science Reviews 17, 1–29.
Almeida, F.F.M., de Brito Neves, B.B., Carneiro, C.D.R., 2000. The origin and evolution of the South America platform. Earth Science Reviews 50, 77–111.
Armstrong-Altrin, J.S., 2015. Evaluation of two multi-dimensional discrimination diagrams from beach and deep sea sediments from the Gulf of Mexico and their application to Precambrian clastic sedimentary rocks. International Geology Review 57, 1446–1461.
Arndt, N.T., 1986. Differentiation of komatiite flows. Journal of Petrology 27, 279–301.
Arndt, N.T., 1994. Archaean komatiites. In: Condie, K.C. (Ed.), Archaean Crustal Evolution. Elsevier, Amsterdam, pp. 11–44.
Arndt, N.T., 2003. Komatiites, kimberlites and boniites. Journal of Geophysical Research 108 (B6), 2293.
Arndt, N.T., Nisbet, E.G., 1982. Komatiites. George Allen and Unwin Publ, UK. 526 pp.
Arndt, N.T., Teixeira, N.A., White, W.M., 1989. Bizarre geochemistry of komatiites from the Crixás greenstone belt, Brazil. Contributions to Mineralogy and Petrology 101, 187–197.
Arndt, N.T., Lesher, C.M., Barnes, S.J., 2008. Komatiites: New York. Cambridge University Press 467 pp.
Baltazar, O.F., Zucchetti, M., 2007. Lithofacies associations and structural evolution of the Archean Rio das Velhas greenstone belt, Quadrilátero Ferrífero, Brazil: a review of the setting of gold deposits. Ore Geology Reviews 32, 1–2.
Barbosa, J.S.F., Sabaté, P., 2004. Archean and Paleoproterozoic crust of the São Francisco Craton, Bahia, Brazil: geodynamic features. Precambrian Research 133, 1–27.
Barnes, S.J., Hill, R.E.T., Gole, M.J., 1988. The perseverance ultramafic complex, Western Australia: the product of a komatiite Lava River. Journal of Petrology 29, 305–331.
Basei, M.A.S., Siga Jr., O., Masquelin, H., Harara, O.M., Reis Neto, J.M., Preciozzi, E.P., 2000. The Dom Feliciano Belt and the Rio de la Plata Craton. In: Cordani, U.G., Milani, E.J., Thomaz Filho, A., Campos, D.A. (Eds.), Tectonic Evolution of South American. 31st International Geological Congress, Rio de Janeiro, pp. 311–334.
Braun, J.J., Pagel, M., Herbillon, A., Rosin, C., 1993. Mobilization and redistribution of REEs and thorium in a syenitic lateritic profile: a mass balance study. Geochimica et Cosmochimica Acta 57, 4419–4434.
Campbell, I.H., 2002. Implications of Nb/U, Th/U and Sm/Nd in plume magmas for the relationship between continental and oceanic crust formation and the development of the depleted mantle. Geochimica et Cosmochimica Acta 66, 1651–1661.
Campos, J.C.S., Carneiro, M.A., 2008. Neoarchean and Paleoproterozoic granitoids marginal to the Jeceaba–Bom Sucesso lineament (SE border of the southern São Francisco craton): genesis and tectonic evolution. Journal of South American Earth Sciences 26, 463–484.
Carneiro, M.A., 1992. O Complexo Metamórfico Bonfim Setentrional (Quadrilátero Ferrífero, MG): Litoestratigrafia e evolução geológica de um segmento de crosta continental do Arqueano. PhD thesis. Instituto de Geociências, Universidade de São Paulo, São Paulo, Brasil 233 pp.
Chavagnac, V., 2004. A geochemical and Nd isotopic study of Barberton komatiites (South Africa): implication for the Archean mantle. Lithos 75, 253–281.
Condie, K.C., 2003. Incompatible element ratios in oceanic basalts and komatiites: tracking deep mantle sources and continental growth rates with time C8–1005. Geochemistry, Geophysics, Geosystems 4, 1–28.
Condie, K., 2015. Changing tectonic settings through time: indiscriminate use of geochemical discriminant diagrams. Precambrian Research 266, 587–591.
Condie, K.C., Aster, R.C., van Hunen, J., 2016. A great thermal divergence in the mantle beginning 2.5 Ga: geochemical constraints from greenstone basalts and komatiites. Geoscience Frontiers 7, 543–553.
Cordani, U.G., Teixeira, W., 2007. Proterozoic accretionary belts in the Amazonian Craton. In: Hatcher Jr., R.D., Carlson, M.P., McBride, J.H. (Eds.), 4-D Framework of Continental Crust. Memoir 220. Geological Society of America, Boulder, CO, pp. 297–320.
Cordani, U.G., Sato, K., Teixeira, W., Tassinari, C.C.G., Basei, M.A.S., 2000. Crustal evolution of the South American platform. In: Cordani, U.G., Milani, E.J., Thomaz Filho, A.,

Campos, D.A. (Eds.), Tectonic Evolution of South American. 31st International Geological Congress, Rio de Janeiro, pp. 19–40.
Cotta, A.J.B., Enzweiler, J., 2009. Quantification of major and trace elements in water samples by ICP–MS and collision cell to attenuate Ar and Cl-based polyatomic ions. Journal of Analytical Atomic Spectrometry 24, 1406–1413.
Cunha, J.C., Fróes, R.J.B., 1994. Komatiitos com textura spinifex do Greenstone belt de Umburanas, Bahia. Série Arquivos Abertos. Companhia Baiana de Pesquisa Mineral e CBPM, Salvador, In 29pp.
Delgado, I.M., Pedreira, A.J.P., Thorman, C.H., 1994. Geology and mineral resources of Brazil: a review. International Geology Review 36, 503–544.
Dorr, J.V.N., 1969. Physiographic, Stratigraphic, and Structural Development of the Quadrilatero Ferrifero, Minas Gerais, Brazil, Professional Paper, Washington, D.C. C6. pp. A1–A110.
Dostal, J., Mueller, W.U., 2004. Komatiite geochemistry. In: Eriksson, P.G., Altermann, W., Nelson, D., Mueller, R., Catuneanu, W.U. (Eds.), The Precambrian Earth: Tempos and Events. Elsevier, Amsterdam, pp. 290–298.
Dostal, J., Mueller, W.U., 2013. Deciphering an Archean mantle plume: Abitibi greenstone belt, Canada. Gondwana Research 23, 493–505.
Eggins, S.M., Woodhead, J.D., Kinsley, L.P.J., Mortimer, G.E., Sylvester, P., McCulloch, M.T., Hergt, J.M., Handler, M.R., 1997. A simple method for the precise determination of ≥40 trace elements in geological samples by ICPMS using enriched isotope internal standardisation. Chemical Geology 134, 311–326.
Fan, J., Kerrich, R., 1997. Geochemical characteristics of aluminium depleted and undepleted komatiites and HFSE-enriched low-Ti tholeiites, western Abitibi greenstone belt: a heterogeneous mantle plume-convergent margin environment. Geochimica et Cosmochimica Acta 61, 4723–4744.
Farina, F., Albert, A., Lana, C., 2015. The Neoarchean transition between medium- and high-K granitoids: clues from the southern São Francisco craton (Brazil). Precambrian Research 266, 375–394.
Frizzo, C., Takai, V., Scarpelli, W., 1991. Auriferous Mineralization at Pitangui, Minas Gerais. In: Ladeira, E.A. (Ed.), Brazil Gold 91. Balkema, Rotterdam, pp. 579–583.
Fuck, R.A., Neves, B.B.B., Schobbenhaus, C., 2008. Rodinia descendants in South America. Precambrian Research 160, 108–126.
Gair, J.E., 1962. Geology and Ore Deposit of the Nova Lima and Rio Acima Quadrangles. United States Geological Survey, Minas Gerais, Brazil. Professional Paper 341-a, p. 67.
Geraldes, M.C., Tavares, A.D., Santos, A.C.D., 2015. An overview of the Amazonian craton evolution: insights for paleocontinental reconstruction. International Journal of Geosciences 6, 1060–1076.
Gruau, G., Tourpin, S., Fourcade, S., Blais, S., 1992. Loss of isotopic (Nd, O) and chemical (REE) memory during metamorphism of komatiites: new evidence from eastern Finland. Contributions to Mineralogy and Petrology 112, 66–82.
Hanson, G.N., Langmuir, C.H., 1978. Experimental trace element geochemistry modelling of major elements in mantle–melt systems using trace element approaches. Geochimica et Cosmochimica Acta 42, 725–741.
Hartmann, L.A., Delgado, I.M., 2001. Craton and orogenic belts of the Brazilian shield and their contained gold deposits. Mineralium Deposita 36, 207–217.
Hartmann, L.A., Endo, I., Suita, M.T.F., Santos, J.O.S., Frantz, J.C., Carneiro, M.A., Mcnaughton, N.J., Barley, M.E., 2006. Provenance and age delimitation of Quadrilátero Ferrífero sandstones based on zircon U–Pb isotopes. Journal of South American Earth Sciences 20, 273–285.
Hartmann, L.A., Santos, J.O.S., McNaughton, N.J., 2008. Detrital zircon U–Pb age data, and Precambrian provenance of the Paleozoic Guaritas formation, southern Brazilian shield. International Geology Review 50, 364–374.
Herzberg, C., 1995. Generation of plume magmas through time - an experimental perspective. Chemical Geology 126, 1–16.
Herzberg, C., O'Hara, M.J., 1998. Phase equilibrium constraints on the origin of basalts, picrites, and komatiites. Earth-Science Reviews 44, 39–79.
Herzberg, C., Condie, K., Korenaga, J., 2010. Thermal history of the earth and its petrological expression. Earth and Planetary Science Letters 292, 79–88.
Hofmann, A.W., 1988. Chemical differentiation of the earth: the relationship between mantle, continental crust, and oceanic crust. Earth and Planetary Science Letters 90, 297–314.
Hofmann, A.W., 1997. Mantle geochemistry: the message from oceanic volcanism. 385, 219–229.
Jahn, B.–.M., Gruau, G., Glikson, A.Y., 1982. Komatiites of the Onverwacht group, S. Africa: REE geochemistry, Sm/Nd age and mantle evolution. Contributions to Mineralogy and Petrology 80, 25–40.
Jayananda, M., Duraiswami, R.A., Aadhiseshan, K.R., Gireesh, R.V., Prabhakar, B.C., Kafoc, Kowe-u, Tushipoklac, Namratha R., 2016. Physical volcanology and geochemistry of Palaeoarchaean komatiite lava flows from the western Dharwar craton, southern India: implications for Archaean mantle evolution and crustal growth. International Geology Review 58, 1569–1595.
Jenson, L.S., 1976. A new method of classifying alkali volcanic rocks. Ontario Division Mineral, Miscellaneous Paper. 66, pp. 22.
Klein, E.L., Moura, C.A.V., 2008. São Luis craton and Gurupi belt (Brazil): possible links with the west Africa craton and surrounding Oan-African belts. In: Pankhurst, R.J., Trouw, R.A.J., Brito Neves, B.B., De Witt, M.J. (Eds.), West Gondwana- pre-Cenozoic Correlations across the South Atlantic Region. Geological Society of London, Special Publication 294, pp. 137–151.
Klein, E.L., Moura, C.A.V., Harris, C., Giret, A., 2005. Reconnaissance stable isotope (C, O, H, S) study of paleoproterozoic gold deposits of the São Luis Craton and Country Rocks, Northern Brazil: implications for gold metallogeny. International Geology Review 47, 1131–1143.
Konnunaho, J.P., Hanski, E.J., Bekker, A., Halkoaho, T.A.A., Hiebert, R.D., Wing, B.A., 2013. The Archean komatiite-hosted, PGE-bearing Ni–Cu sulfide deposit at Vaara, eastern Finland: evidence for assimilation of external sulfur and post-depositional desulfurization. Mineralium Deposita 48, 967–989.
Lana, C., Alkmim, F.F., Armstrong, R., Scholz, R., Romano, R., Nalini Jr., H.A., 2013. The ancestry and magmatic evolution of Archaean TTG rocks of the Quadrilátero Ferrífero province, southeast Brazil. Precambrian Research 231, 157–173.
Le Bas, M.J., Maitre, R.W.L., Streckeisen, A., Zanettin, B., 1986. A chemical classification of volcanic rocks based on the total alkali–silica diagram. Journal of Petrology 27, 745–750.
Lécuyer, C., Gruau, G., Anhauesser, C.R., Fourcade, S., 1994. The origin of fluids and the effects of metamorphism on the primary chemical compositions of Barberton komatiites: new evidence from geochemical (REE) and isotopic (Nd, O, H, $^{39}Ar/^{40}Ar$) data. Geochimica et Cosmochimica Acta 58, 969–984.
Ledru, P., Mile'si, J.P., Johan, V., Sabaté, P., Maluski, H., 1997. Foreland basins and gold–bearing conglomerates: a new model for the Jacobina Basin (São Francisco province, Brazil). Precambrian Research 86, 155–176.
Lesher, C.M., Stone, W.E., 1996. Exploration geochemistry of komatiites. In: Wyman, D.A. (Ed.), Igneous Trace Element Geochemistry: Applications for Massive Sulphide Exploration. Geological Association of Canada vol. 12, pp. 153–204 Short Course.
Liang, Q., Jing, H., Gregoire, D.C., 2000. Determination of trace elements in granites by inductively coupled plasma mass spectrometry. Talanta 51, 507–513.
Lobato, L., Ribeiro–Rodrigues, L., Vieira, F., 2001a. Brazil's premier gold province. Part II: geology and genesis of gold deposits in the Archean Rio das Velhas greenstone belt, Quadrilátero Ferrífero. Mineralium Deposita 36, 249–277.
Lobato, L., Ribeiro–Rodrigues, L., Zucchetti, M., Noce, C., Baltazar, O., da Silva, L., Pinto, C., 2001b. Brazil's premier gold province. Part I: the tectonic, magmatic, and structural setting of the Archean Rio das Velhas greenstone belt, Quadrilátero Ferrífero. Mineralium Deposita 36, 228–248.
Ludden, J., Gélinas, L., Trudel, P., 1982. Archean metavolcanics from the Rouyn–Noranda district, Abitibi Greenstone Belt, Quebec. 2. Mobility of trace elements and petrogenetic constraints. Canadian Journal of Earth Sciences 19, 2276–2287.
Machado, N., Noce, C.M., Ladeira, E.A., Belo de Oliveira, O., 1992. U–Pb geochronology of Archean magmatism and Proterozoic metamorphism in the Quadrilátero Ferrífero, southern São Francisco Craton, Brazil. Geological Society of America Bulletin 104, 1221–1227.
Manikyamba, C., Kerrich, R., Polat, A., Saha, A., 2013. Geochemistry of two stratigraphically-related ultramafic (komatiite)layers from the Neoarchean Sigegudda greenstone terrane,Western Dharwar craton, India: evidence for compositional diversity inArchean mantle plumes. Lithos 177, 120–135.
Mascarenhas, J.S., 1981. O embasamento Precambriano no Estado da Bahia e sua gênese. Cráton São Francisco. Salvador, 5. CBPM, Série Arquivos Abertos.
McDonough, W.F., Sun, S.s., 1995. The composition of the earth. Chemical Geology 120, 223–253.
Menezes Leal, A.B., Santos, A.L.D., Leal, L.R.B., Cunha, J.C., 2015. Geochemistry of contaminated komatiites from the Umburanas greenstone belt, Bahia State, Brazil. Journal of South American Earth Sciences 61, 1–13.
Middlemost, E.A.K., 1989. Iron oxidation ratios, norms and the classification of volcanic rocks. Chemical Geology 77, 19–26.
Mole, D.R., Fiorentini, M.L., Thebaud, N., Cassidy, K.F., McCuaig, T.C., Kirkland, C.L., Romano, S.S., Doublier, M.P., Belousova, E.A., Barnes, S.J., Miller, J., 2014. Archean komatiite volcanism controlled by the evolution of early continents. Proceedings of the National Academy of Sciences 111, 10083–10088.
Moreira, H., Lana, C., Nalini Jr., H.A., 2016. The detrital zircon record of an Archaean convergent basin in the Southern São Francisco Craton, Brazil. Precambrian Research 275, 84–99.
Moreno, J.A., Baldim, M.R., Semprich, J., Oliveira, E.P., Verma, S.K., Teixeira, W., 2017. Geochronological and geochemical evidences for extension-related Neoarchean granitoids in the southern São Francisco Craton, Brazil. Precambrian Research 294, 322–343.
Noce, C.M., Dantas, E.L., Lobato, L.M., Zucchetti, M., Baltazar, O.F., 2002. Múltiplos eventos de vulcanismo no greenstone belt Rio das Velhas, Quadrilátero Ferrífero (MG): novos dados U–Pb, implicações geotectônicas e metalogenéticas. 41th Congresso Brasileiro de Geologia. Sociedade Brasileira de Geologia, João Pessoa, p. 522.
Noce, C.M., Zucchetti, M., Baltazar, O.F., Armstrong, R., Dantas, E.L., Renger, F.E., Lobato, L.M., 2005. Age of felsic volcanism and the role of ancient continental crust in the evolution of the Neoarchean Rio das Velhas greenstone belt (Quadrilátero Ferrífero, Brazil): U–Pb zircon dating of volcaniclastic graywackes. Precambrian Research 141, 67–82.
Oliveira, E.P., McNaughton, N.J., Armstrong, R., 2010. Mesoarchaean to Palaeoproterozoic growth of the northern segment of the Itabuna-Salvador-Curaçá Orogen, São Francisco Craton, Brazil. In: Kusky, T.M., Zhai, M.-G., Xiao, W. (Eds.), The Evolving Continents: Understanding Processes of Continental Growth. Geological Society, London, Special Publications 338, pp. 263–286.
Oliveira, E.P., Souza, Z.S., McNaughton, N.J., Lafon, J.M., Costa, F.G., Figueiredo, A.M., 2011. The Rio Capim volcanic–plutonic–sedimentary belt, São Francisco Craton, Brazil: geological, geochemical and isotopic evidence for oceanic arc accretion during Palaeoproterozoic continental collision. Gondwana Research 19, 735–750.
O'Rourke, J.E., 1957. The Stratigraphy of Metamorphic Rocks of the Rio de Pedras and Gandarela Quadrangles, Minas Gerais, Brazil. (PhD thesis). University of Winscosin, Winscosin, p. 106.
Oyhantçabal, P., Siegesmund, S., Wemmer, K., 2011. The Río de Plata Craton: a review of units, boundaries, ages and isotopic significance. International Journal of Earth Sciences 100, 201–220.
Parman, S.W., Grove, T.L., 2004. Petrology and geochemistry of Barberton komatiites and basaltic komatiites: evidences of Archean fore-arc magmatism. In: Kusky, T.M. (Ed.), Precambrian Ophiolites and Related Rocks. Developments in Precambrian Geology vol. 13, pp. 539–565.

Parman, S.W., Dann, J.C., Grove, T.L., de Wit, M.J., 1997. Emplacement conditions of komatiite magmas from the 3.49 Ga Komati Formation, Barberton Greenstone Belt, South Africa1. Earth and Planetary Science Letters 150, 303–323.
Parman, S.W., Grove, T.L., Dann, J.C., De Wit, M.J., 2004. A subduction origin for komatiites and cratonic lithospheric mantle. South African Journal of Geology 107, 107–118.
Pearce, T.H., 1968. A contribution to the theory of variations diagrams. Contributions to Mineralogy and Petrology 19, 142–157.
Pearce, J.A., 2008. Geochemicalfingerprinting of oceanic basalts with applications toophiolite classification and the search for Archean oceanic crust. Lithos 100, 14–48.
Polat, A., Kerrich, R., 2000. Archean greenstone belt magmatism and the continental growth–mantle evolution connection: constraints from Th–U–Nb–LREE systematics of the 2.7 Ga Wawa subprovince, Superior Province, Canada. Earth and Planetary Science Letters 175, 41–54.
Polat, A., Kerrich, R., Wyman, D.A., 1999. Geochemical diversity in oceanic komatiites and basalts from the late Archean Wawa greenstone belts, Superior Province, Canada: trace element and Nd isotope evidence for a heterogeneous mantle. Precambrian Research 94, 139–173.
Rajamani, V., Shivkumar, K., Hanson, G.N., Shirey, S.B., 1985. Geochemistry and Petrogenesis of Amphibolites, Kolar Schist Belt, South India: evidence for Komatiitic magma derived by low percentages of melting of the mantle. Journal of Petrology 26, 92–123.
Rapela, C.W., Pankhurst, R.J., Casquet, C., Fanning, C.M., Baldo, E.G., González-Casado, J.M., Galindo, C., Dahlquist, J., 2007. The Río de la Plata craton and the assembly of SW Gondwana. Earth Science Reviews 83, 49–82.
Roeder, P.L., Emslie, R.F., 1970. Olivine–liquid equilibrium. Contributions to Mineralogy and Petrology 29, 275–289.
Romano, A., 2007. Programa Geologia do Brasil. Folha Pará de Minas, SE- 23-Z-CI. Escala 1: 100.000, relatório final. UFMG - CPRM. Belo Horizonte 72p.
Romano, R., Lana, C., Alkmim, F.F., Stevens, G., Armstrong, R., 2013. Stabilization of the southern portion of the São Francisco craton, SE Brazil, through a long–lived period of potassic magmatism. Precambrian Research 224, 143–159.
Sadowski, 2000. The São Luís Craton and the Gurupi Fold Belt. In: Cordani, U.G., Milani, E.J., Thomaz Filho, A., Campos, D.A. (Eds.), Tectonic Evolution of South American. 31st International Geological Congress, Rio de Janeiro, pp. 97–100.
Saha, A., Manikyamba, C., Santosh, M., Ganguly, S., Khelen, A.C., Subramanyam, K.S.V., 2015. Platinum group elements (PGE) geochemistry of komatiites and boninites from Dharwar Craton, India: implications for mantle melting processes. Journal of Asian Earth Sciences 105, 300–319.
Sánchez Bettucci, L., Peel, E., Oyhantçabal, P., 2010. Precambrian geotectonic units of the Río de La Plata craton. International Geology Review 32, 50–78.
Santos, J.O.S., Hartmann, L.A., Gaudette, H.E., Groves, D.I., McNaughton, N.J., Flecher, I.R., 2000. A new understanding of the provinces of the Amazon Craton based on integration of field mapping and U–Pb and Sm–Nd geochronology. Gondwana Research 3, 489–506.
Schrank, A., Souza Filho, C.R., Roig, H.L., 1990. Novas Observações sobre as Rochas Ultramáficas do Grupo Quebra Osso e Formação Córrego dos Boiadeiros, Greenstone Belt Rio Velhas – MG. Cadernos Instituto de Geociências/UNICAMP 1, 6–29.
Silva, P.M., 2016. Geoquimica e geocronologia das rochas metavulcanicas, metaplutonicas e metassedimentares do greenstone belt de Pitangui. MG. Master dissertation. Institute of Geosciences, University of Campinas, Brazil.
Silva, P.M., Amaral, W.S., Oliveira, E.P., Camargo, I.M., 2017. Neoarchean evolution of the Pitangui greenstone belt, southern São Francisco Craton, Brazil. Journal of South American Earth Sciences under review.
Soares, M.B., Corrêa Neto, A.V., Zeh, A., Cabral, A.R., Pereira, L.F., Prado, M.G.B., Almeida, A.M., Manduca, L.G., Silva, P.H.M., Mabub, R.O.A., Schlichta, T.M., 2017. Geology of the Pitangui greenstone belt, Minas Gerais, Brazil: stratigraphy, geochronology and BIF geochemistry. Precambrian Research. http://dx.doi.org/10.1016/j.precamres.2017.01.008.
Sproule, R.A., Lesher, C.M., Ayer, J.A., Thurston, P.C., Herzberg, C.T., 2002. Spatial and temporal variations in the geochemistry of komatiites and komatiitic basalts in the Abitibi greenstone belt. Precambrian Research 115, 153–186.
Stiegler, M.T., Lowe, D.R., Byerly, G.R., 2010. The petrogenesis of volcaniclastic komatiites in the Barberton Greenstone Belt, South Africa; a textural and geochemical study. Journal of Petrology 51, 947–972.
Tassinari, C.C.G., Macambira, M.J.B., 1999. Geochronological provinces of the Amazonian Craton. Episodes 22, 174–182.
Tassinari, C.C.G., Bettencourt, J.S., Geraldes, M.J.B., Macambira, M.J.B., Lafon, J.M., 2000. The Amazonian Craton. In: Cordani, U.G., Milani, E.J., Thomaz Filho, A., Campos, D.A. (Eds.), Tectonic Evolution of South American. 31st International Geological Congress, Rio de Janeiro, pp. 41–96.
Teixeira, W., Figueiredo, M.C.H., 1991. An outline of Early Proterozoic crustal evolution in the São Francisco craton, Brazil: a review. Precambrian Research 53, 1–22.
Teixeira, W., Tassinari, C.C.G., Cordani, U.G., Kawashita, K., 1989. A review of the geochronology of the Amazonian Craton: tectonic implications. Precambrian Research 42, 213–227.
Teixeira, W., Carneiro, M.A., Noce, C.M., Machado, N., Sato, K., Taylor, P.N., 1996. The oldest rocks on earth: Pb, Sr and Nd isotope constraints on the Archaean evolution of gneissic–granitoid complexes in the southern São Francisco craton, Brazil. Precambrian Research 78, 151–164.
Teixeira, W., Geraldes, M.C., Matos, R., Ruiz, A.S., Saes, G., Vargas–Mattos, G., 2010. A review of the tectonic evolution of the Sunsás belt, SW Amazonian Craton. Journal of South American Earth Sciences 29, 47–60.
Teixeira, W., Ávila, C.A., Dussin, I.A., Corrêa Neto, A.V., Bongiolo, E.M., Santos, J.O., Barbosa, N.S., 2015. A juvenile accretion episode (2.35–2.32 Ga) in the Mineiro belt and its role to the Minas accretionary orogeny: zircon U–Pb–Hf and geochemical evidences. Precambrian Research 256, 148–169.
Teixeira, W., Oliveira, E.P., Marques, L.S., 2017a. The nature and evolution of the Archean Crust of the São Francisco Craton. In: Heilbron, M., Cordani, U.G., Alkmim, F.F. (Eds.), São Francisco Craton, Eastern Brasil: Tectonic Genealogy of a Miniature Continent, Regional Geology Review Series. Springer International:pp. 29–56. http://dx.doi.org/10.1007/978–3–319-01715-0_3.
Teixeira, W., Oliveira, E.P., Peng, P., Dantas, E.L., Hollanda, M.H.B.M., 2017b. U-Pb geochronology of the 2.0 Ga Itapecerica graphite-rich supracrustals uccession in the São Francisco Craton: tectonic matches with the NorthChina Craton and paleogeographic inferences. Precambrian Research 293, 91–111.
Tohver, E., Teixeira, W., van der Plujm, B., Geraldes, M.C., Bettencourt, J.S., 2006. Restored transect across the exhumed Grenville Orogen of Laurentia and Amazonia, with implications for crustal architecture. Geology 34, 669–672.
Tohver, E., Bettencourt, J.S., Tosdal, R., Mezger, K., Leite, W.B., Payolla, B.L., 2004. Terrane transfer during the Grenville orogeny: tracing the Amazonian ancestry of southern Appalahian basement through Pb and Nd isotopes. Earth Planetary Science Letters 228, 161–176.
Trompette, R., 1994. Geology of Western Gondwana (2000–500 ma). Pan-African-Brasiliano Aggregation of South America and Africa. Balkema, Rotterdam.
Vendemiatto, M.A., Enzweiler, J., 2001. Routine control of accuracy in silicate rock analysis by X–ray fluorescence spectrometry. Geostandards Newsletter 25, 283–291.
Verma, S.P., 2010. Statistical evaluation of bivariate, ternary and discriminant function tectonomagmatic discrimination diagrams. Turkish Journal of Earth Sciences 19, 185–238.
Verma, S.P., 2015. Present state of knowledge and new geochemical constraints on the central part of the Mexican Volcanic Belt and comparison with the Central American Volcanic Arc in terms of near and far trench magmas. Turkish Journal of Earth Sciences 24, 399–460.
Verma, S.P., Agrawal, S., 2011. New tectonic discrimination diagrams for basic and ultrabasic volcanic rocks through log-transformed ratios of high field strength elements and implications for petrogenetic processes. Revista Mexicana de Ciencias Geológicas 28, 24–44.
Verma, S.P., Armstrong-Altrin, J.S., 2016. Geochemical discrimination of siliciclastic sediments from active and passive margin settings. Sedimentary Geology 332, 1–12.
Verma, S.P., Rivera-Gómez, M.A., 2013. Computer programs for the classification and nomenclature of igneous rocks. Episodes 36, 115–124.
Verma, S.P., Verma, S.K., 2013. First 15 probability-based multi-dimensional discrimination diagrams for intermediate magmas and their robustness against post emplacement compositional changes and petrogenetic processes. Turkish Journal of Earth Sciences 22, 931–995.
Verma, S.P., Guevara, M., Agrawal, S., 2006. Discriminating four tectonic settings: five new geochemical diagrams for basic and ultrabasic volcanic rocks based on log — ratio transformation of major–element data. Journal of Earth System Science 115, 485–528.
Verma, S.K., Pandarinath, K., Verma, S.P., 2012. Statistical evaluation of tectonomagmatic discrimination diagrams for granitic rocks and proposal of new discriminant–function–based multi–dimensional diagrams for acid rocks. International Geology Review 54, 325–347.
Verma, S.P., Pandarinath, K., Verma, S.K., Agrawal, S., 2013. Fifteen new discriminant–function–based multi–dimensional robust diagrams for acid rocks and their application to Precambrian rocks. Lithos 168–169, 113–123.
Verma, S.K., Oliveira, E.P., Verma, S.P., 2015a. Plate tectonic settings for Precambrian basic rocks from Brazil by multidimensional tectonomagmatic discrimination diagrams and their limitations. International Geology Review 57, 1566–1581.
Verma, S.P., Verma, S.K., Oliveira, E.P., 2015b. Application of 55 multi–dimensional tectonomagmatic discrimination diagrams to Precambrian belts. International Geology Review 57, 1365–1388.
Verma, S.P., Rivera-Gómez, M.A., Díaz-González, L., Quiroz-Ruiz, A., 2016. Log-ratio transformed major-element based multidimensional classification for altered high-Mg igneous rocks. Geochemistry, Geophysics, Geosystems 17, 1–18.
Verma, S.P., Rivera-Gomez, M.A., Díaz-González, L., Pandarinath, K., Amezcua-Valdez, A., Rosales-Rivera, M., Verma, S.K., Quiroz-Ruiz, A., ArmstrongAltrin, J.S., 2017. Multidimensional classification of magma types for altered igneous rocks and application to their tectonomagmatic discrimination and igneous provenance of siliciclastic sediments. Lithos 278–281, 321–330.
Vial, D.S., Abreu, G.C., Schubert, G., Ribeiro-Rodrigues, L.C., 2007. Smaller gold deposits in the Archean Rio das Velhas greenstone belt, Quadrilátero Ferrífero, Brazil. Ore Geology Reviews 32, 651–673.
Waterton, P., Person, D.G., Kjarsgaard, B., Hulbert, L., Locock, A., Parman, S., David, D., 2017. Age, origin, and thermal evolution of the ultra-fresh ~1.9 Ga Winnipegosis komatiites, Manitoba, Canada. Lithos 268–271, 114–130.
Zucchetti, M., Lobato, L.M., Baltazar, O.F., 2000a. Volcanic and volcaniclastic features in Archean rocks and their tectonic environment, Rio das Velhas Greenstone Belt, Quadrilátero Ferrífero, MG. Brazil. Revista Brasileira de Geociências 30, 388–392.
Zucchetti, M., Lobato, L.M., Baars, F.J., 2000b. Genetically diverse basalt geochemical signatures developed in the Rio das Velhas Greenstone Belt, Quadrilátero Ferrífero, Minas Gerais, Brazil. Revista Brasileira de Geociencias 30, 397–402.